日本磁気学会
ISSN 2432-0250
Journal of the Magnetics Society of Japan
Electronic Journal URL: https://www.jstage.jst.go.jp/browse/msjmag

Vol.50 No.1　2026

Journal

Magnetic Recording

Hard and Soft Magnetic Materials

Thin Films, Fine Particles, Multilayers, Superlattices

JOURNAL OF THE MAGNETICS SOCIETY OF JAPAN

Vol.50 No.1 2026

日本磁気学会

ISSN 2432-0250

HP: http://www.magnetics.jp/ e-mail: msj@bj.wakwak.com
Electronic Journal: http://www.jstage.jst.go.jp/browse/msjmag

TPM-2-08s25

HcJの3σ/Ave. 0.2%[※1]を実現
渦電流補正方法[※2]も確立済

試料測定磁界
max 15Tesla

最大試料直径
10mm

パルス励磁型磁気特性測定装置

永久磁石および磁性体粉末を固形化した高磁化試料のヒステリシス曲線の自動測定および描画、SPD (Singuler Point Detection) 測定が可能です。(RT～+200℃)

※1　電気学会資料 MAG-18-088 参照
※2　電気学会資料 MAG-07-011 参照

NdFeB(sintered) 測定例

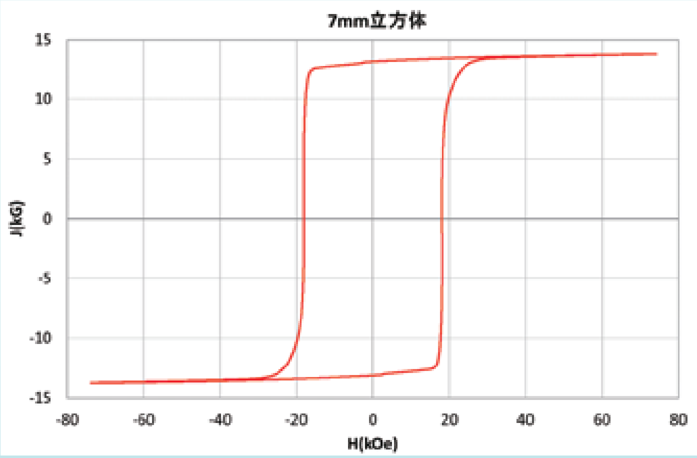

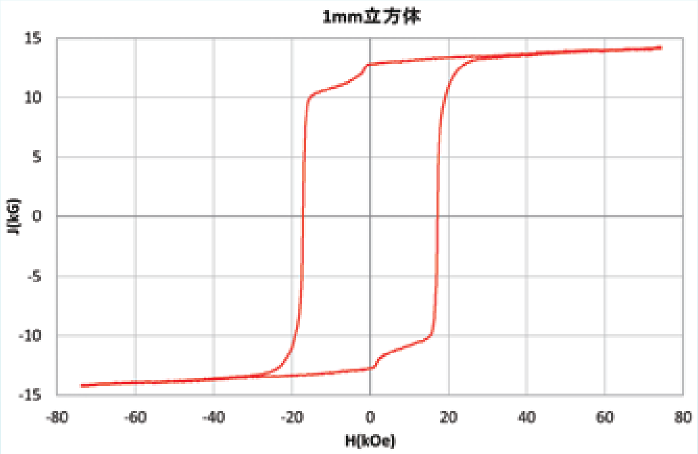

1mm 立方体測定用検出コイルはオプション品です

東英工業では他に振動試料型磁力計(VSM)、直流自記磁束計(JIS C2501 準拠)を始め、各種磁気測定装置を取り揃えております。ぜひお問い合わせ下さい

TOEI 東英工業株式会社
http://www.toeikogyo.co.jp

〒194-0035 東京都町田市忠生1-8-13
TEL:042-791-1211 FAX:042-792-0490
E-mail:sales@toeikogyo.co.jp

INDEX

Journal of the Magnetics Society of Japan

Vol. 50, No. 1

Electronic Journal URL: https://www.jstage.jst.go.jp/browse/msjmag

CONTENTS

Magnetic Recording

Hard and Soft Magnetic Materials

Thin Films, Fine Particles, Multilayers, Superlattices

J. Magn. Soc. Jpn., **50**, 1-5 (2026) <Paper>

A Study on Error Correction for Domain Wall Motion Memory

Yasuaki Nakamura, Madoka Nishikawa, Yoshihiro Okamoto
Graduate School of Science and Engineering, Ehime University, *3 Bunkyo-cho, Matsuyama, Ehime, 790-8577, Japan*

Vertical domain wall motion memory, which uses magnetic pillars composed of artificial ferromagnets with diameters of several tens of nanometers, is gaining attention as a next-generation high-capacity memory solution. In this memory device, where domain walls move vertically, deletion and insertion errors can occur due to fluctuations in domain wall displacement, which are influenced by the write and drive currents. In this study, we construct a read/write (RW) channel model incorporating probabilistic domain wall motion memory with a 512-bit pillar structure and evaluate an error correction system using a Levenshtein code concatenated with a Reed–Solomon (RS) code. The results show that, in the scheme where each pillar is divided into prespecified blocks and Levenshtein coding is applied, the frame error rate performance improves as the number of blocks increases. Furthermore, it was found that the decoding can achieve the frame error rate (FER) less than 10^{-3} when the standard deviation of domain wall displacement variation is reduced to 0.042 or lower.

Keywords: domain wall motion memory, deletion/insertion errors, error correction system, Levenshtein code, Reed–Solomon (RS) code

1. Introduction

The vertical domain wall motion memory [1)-3)], which stores information bits by forming magnetic domains representing digital values "0" and "1" within magnetic pillars composed of artificial ferromagnetic materials, is attracting attention as a next-generation storage device due to its high integration density and non-volatility. However, since this type of memory writes and reads information by moving domain walls using write and drive currents, variations in these currents may cause the domain walls to deviate from their intended positions [2)], potentially resulting in deletion errors by skipping over a bit or insertion errors by reading the same bit twice. To correct such deletion and insertion errors, we apply the Levenshtein code [3)]. In addition, we construct the frame by concatenating the Reed-Solomon (RS) code [4)] to the Levenshtein code to correct the errors beyond the ability of the Levenshtein code alone.

In this paper, we model a read/write (R/W) channel that includes deletion and insertion errors caused by fluctuations of domain wall motion in the memory. And we evaluate error correction systems in which Levenshtein code is concatenated with an RS code, focusing on their tolerance to the standard deviation of domain wall motion variation.

2. R/W channel of domain wall motion memory

Figure 1 shows the vertical domain wall motion memory proposed in Reference 1. (a) of the figure shows the memory array, where the pillar length L_p is 8 bits with word and bit lines. And (b) of the figure shows the single pillar. The underlayer is a heavy metal-based conduction pillar that serves as the word line for data writing. A cylindrical magnetic pillar is an artificial ferromagnet composed of ferromagnetic multilayers with different magnetic properties. The blue, green, and yellow layers of the magnetic pillar represent a pinning layer with a sufficiently large uniaxial anisotropy constant with perpendicular magnetic anisotropy, a strong coupling layer with sufficiently large exchange stiffness constant and large uniaxial anisotropy constant, and a weak coupling layer with non-ferromagnet with sufficiently weak exchange stiffness constant, respectively. The magnetic tunneling junction (MTJ) on the top, which works as a reader, consists of a fixed layer, a tunnel oxide layer, and a strong coupling layer.

In this magnetic pillar structure in which memory cells equivalent to multiple bits are stacked in a cylinder, the magnetic domain wall displacement occurs each time the magnetic domain wall moves by one channel bit. Figure 2 shows an example of domain wall motion in an R/W channel model, where L_p is 8 bits, and the standard deviation of domain wall motion distance σ_{DW} normalized by a channel bit length L_{cb} is 0.1. The vertical and horizontal axes indicate the domain wall position normalized by L_{cb} and the time normalized by the channel bit interval T_{cb}, respectively. The recording information bits are shown on the lower left of the figure, and the reproducing information bits are shown in the upper right of the figure. The blue circle symbols indicate movements within the allowable range, and the red cross symbols indicate movements outside the range. The magnetic domain wall beneath the third recorded information bit "1" at the bottom left of the figure moves too slowly at $t/T_{cb} = 10$ not to reach $x/L_{cb} = 7$, causing the second information bit "0" to be reproduced again, which results in an “insertion error”. Conversely, the magnetic domain wall beneath the sixth recorded information bit "0" advances too far at $t/T_{cb} = 13$, exceeding $x/L_{cb} = 8$, which causes it to be overwritten and erased by the

---

Corresponding author: Yasuaki Nakamura (e-mail: nakamura.yasuaki.mj@ehime-u.ac.jp).

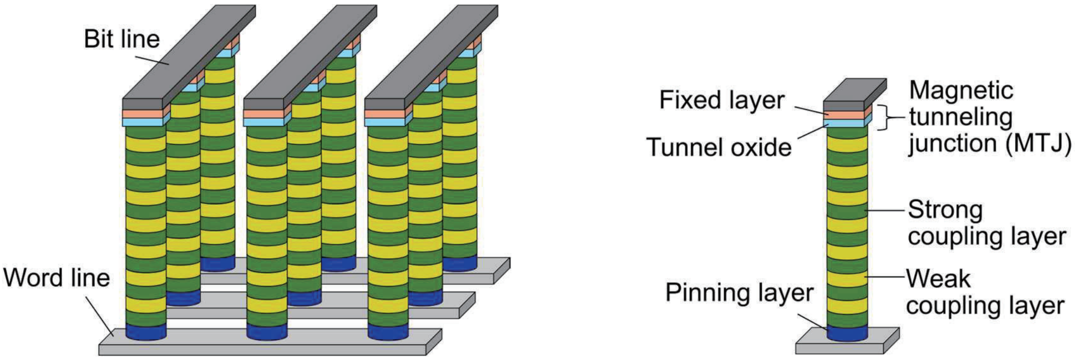

(a) Memory array (b) Single pillar

Fig. 1 Vertical domain wall motion memory with 8 bits per pillar. (a) Memory array with word and bit lines. (b) Single pillar.

seventh recorded information bit "1", resulting in a “deletion error”.

As described above, deletion and insertion errors may occur in the domain wall motion memory, and robust correction schemes are required to correct these errors. To directly evaluate the Levenshtein code for the kind of errors in the domain wall motion memory, the additive white Gaussian noise (AWGN) was not added as a system noise. We think that a system noise may be generated in the reading part, such as the magnetic tunnel junction.

3. Error correction system

3.1 Deletion and insertion error correction

A Levenshtein code [3)] is defined as a code that satisfies the following equation (1) for a binary codeword $\boldsymbol{c} = \{c_1, c_2, \cdots, c_{n_c}\}$ of length n_c.

$$\sum_{i=1}^{n_c} i \cdot c_i \ (\mathrm{mod}\ M) \equiv 0 \tag{1}$$

This code can correct single deletion/insertion/inversion errors in a codeword by knowing the unit length of the recovered codeword in advance. Here, $M \geq 2n_c$, M set to twice the n_c in this study, and the codeword $\boldsymbol{c}$ is defined as follows using the information bits $\boldsymbol{b} = \{b_1, b_2, \cdots, b_{n_b}\}$ before encoding and the check bits $\boldsymbol{p} = \{p_1, p_2, \cdots, p_{n_p}\}$:

$$c_i = \begin{cases} b_{i-\lceil \log_2 i \rceil} & (i \neq n_c \cap i \neq 2^0, 2^1, \cdots, 2^{n_p-2}) \\ p_{\log_2(i)+1} & (i = 2^0, 2^1, \cdots, 2^{n_p-2}) \\ p_{n_p} & (i = n_c) \end{cases} \tag{2}$$

Note that $n_c = n_b + n_p$. Figure 3 shows the codeword structure of the Levenshtein code. As illustrated in the figure, check bits are inserted at positions corresponding to powers of two, i.e., $2^0, 2^1, \cdots, 2^{n_p-2}$, and at n_c, the end of codeword, in accordance with equation (2). Here, check bits $\boldsymbol{p}$ is determined to satisfy equation (1) as follows:

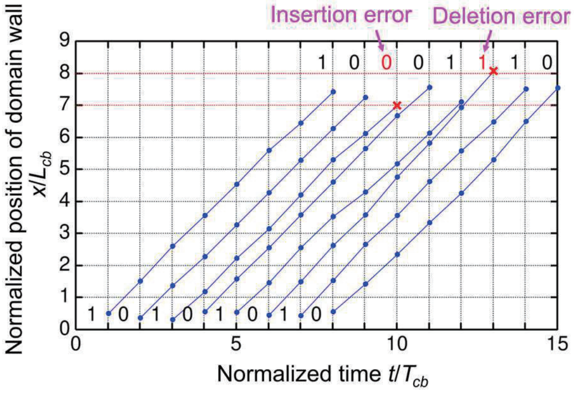

Fig. 2 Domain wall motion in an R/W channel model, where L_p is 8 bits and σ_{DW} is 0.1. Blue circles indicate movements within allowable range, and red crosses indicate movements outside allowable range.

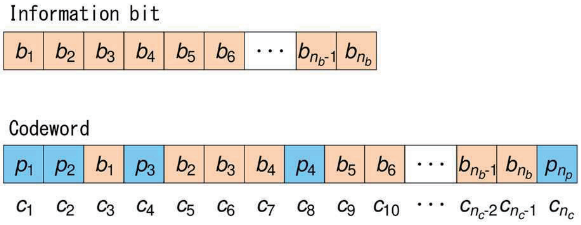

Fig. 3 Codeword $\boldsymbol{c}$ consists of information bits $\boldsymbol{b} = \{b_1, b_2, \cdots, b_{n_b}\}$ before encoding and check bits $\boldsymbol{p} = \{p_1, p_2, \cdots, p_{n_p}\}$.

$$\sum_{\substack{i=1 \\ i \neq 2^0, 2^1, \cdots, 2^{n_p-2}}}^{n_c-1} i \cdot b_i + \sum_{j=0}^{n_p-2} p_{j+1} \cdot 2^j + p_{n_p} \cdot n \ \ (\mathrm{mod}\ M) \equiv 0 \tag{3}$$

For decoding, it is necessary to know the unit length of

Table 1 Number of pillar divisions N_d and maximum number of corrections.

N_d	Length of codeword	η_L	Maximum number of corrections
0	508	0.97	1
2	252	0.95	2
4	124	0.91	4
8	60	0.83	8

the reproduced codeword in advance. However, since the Levenshtein code applied here can only correct a single deletion or insertion error, a 4-bit marker "0011" is appended to the sequence after Levenshtein encoding to allow detection of deviations of up to one channel bit. In this study, marker detection is carried out using correlation. In the reproduced data sequence, whether a deletion or insertion error occurs is identified on a codeword-by-codeword basis using the marker as a reference, and error correction is performed. However, if a deletion or insertion error of two or more channel bits is detected, or if the marker cannot be located, the error correction using the Levenshtein code is not performed.

Here, let us assume that the cylindrical holes in 3D-NAND [6] are used to fabricate the magnetic pillars, and that it is possible to manufacture 3D-NAND with 512 or more stacked layers, i.e., $Lp = 512$. Then, with $n_c = 508$ (i.e., $N_{ab} - 4$) and $n_p = 10$, the encoding rate after Levenshtein encoding, including the 4-bit marker, is given by $\eta_L = (508 - 10)/512 = 0.973$.

In this paper, to increase the number of deletion or insertion errors that can be tolerated within a single magnetic pillar, the information recorded in one pillar is divided into N_d blocks, each of which is Levenshtein-encoded and appended with a marker. When $N_d = 0$, this indicates that Levenshtein encoding is applied without division. Table 1 shows the coding rate and the maximum number of correctable deletion, insertion, and inversion errors when a single frame is divided with $Lp = 512$. As shown in the table, increasing N_d reduces the coding rate, but is expected to increase the number of correctable deletion and insertion errors per frame.

3.2 One-pillar correction with RS code concatenated

Since the Levenshtein code can correct only a single deletion or insertion error per codeword, failure to correct such an error may cause a large portion of the codeword to become errors, resulting in a burst error. To address this, an RS code, which is robust against burst errors, is concatenated as an outer code to the Levenshtein code.

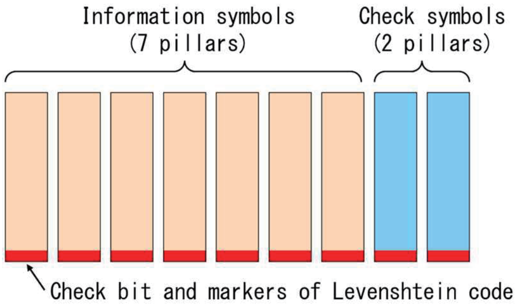

Fig. 4 Codeword structure of RS code. To enable error correction for one pillar uses, two check pillars are added to seven information pillars across nine pillars.

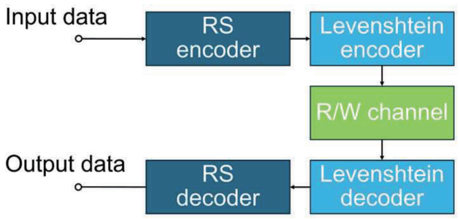

Fig. 5 Block diagram of error correction system using Levenshtein code concatenated with RS code.

The RS code is a block code with an algebraic structure that converts multiple information bits into information symbols (1 symbol = m bits) defined over a finite field (Galois field (2^m)) and can correct t symbol errors by adding $2t$ check symbols. Note that the codeword symbol length n_{RS} after RS coding is $n_{RS} \leq (2^m - 1)$.

In this paper, to enable error correction for one pillar using the RS code, two check pillars are added to the seven information pillars across nine pillars. Figure 4 shows the code structure of the one-pillar correction system using a Levenshtein code concatenated with an RS code. Here, the number of bits that can be recorded per pillar is determined by Lp. Therefore, the number of channel bits per pillar available for the RS code is calculated by subtracting the check bits and markers introduced by the Levenshtein code, considering the division into N_d blocks, from Lp. The Galois field GF(2^9) is used to encode nine pillars simultaneously with the RS code which has the primitive polynomial $x^9 + x^8 + x^5 + x^4 + 1$. For each element in finite field GF(2^9), we associate a power representation with a vector representation using this primitive polynomial. Consequently, the overall coding rate, considering the RS code, the Levenshtein code, and the markers, is approximately equal to η_L from Table 1 multiplied by the RS code rate $\eta_{RS} = 7/9$. Therefore, as shown in Fig. 5, the error correction system first performs RS encoding and then Levenshtein encoding.

3.3 Performance evaluation

Figure 6 shows the flame error rate (FER) performance for σ_{DW}. Note that one frame contains seven pillars as information bits, and error correction using the RS code processes nine pillars. A total of 10,000

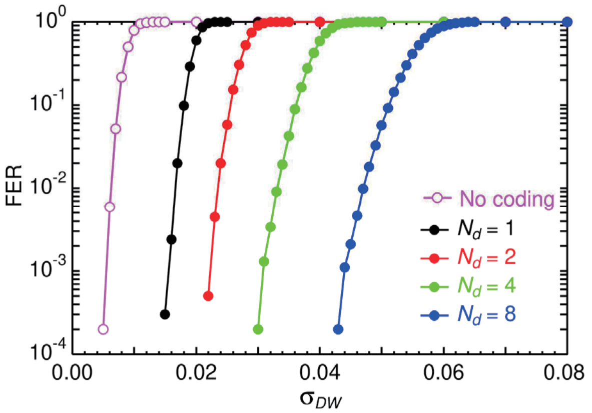

Fig. 6 FER performance for σ_{DW}. Total of 10,000 frames are used.

frames is used. To increase the number of deletion or insertion errors that can be corrected within a single pillar, each pillar is divided into N_d blocks, a Levenshtein encoded, and a 4-bit marker is added. The ●, ●, ●, ● symbols show the FER performances when N_d is 0, 2, 4, and 8, respectively. For comparison, the FER performance without coding are shown by ○ symbols. As can be seen from the figure, increasing N_d makes the system more tolerant to larger σ_{DW}. It was found that the decoding can achieve the FER less than 10^{-3} when $\sigma_{DW} \leq 0.014$ for $N_d = 0$, $\sigma_{DW} \leq 0.021$ for $N_d = 2$, $\sigma_{DW} \leq 0.029$ for $N_d = 4$, and $\sigma_{DW} \leq 0.042$ for $N_d = 8$.

4. Short pillar model

It has become clear that the cumulative fluctuation in domain wall displacement increases as the number of accumulated bits in a single pillar increase, compared to the previous long pillar model with $Lp = 512$ bits. Therefore, we consider a short pillar model with $Lp = 8$ bits (i.e., 1 byte). In this short pillar model, since the pillar is short at 8 bits, error correction employs only RS code without Levenshtein code.

Figure 7 shows the RS coding configuration without Levenshtein code in the short pillar model. Since $L_p = 8$, the RS code is constructed using the Galois field of GF(2^8) which has the primitive polynomial $x^8 + x^7 + x^5 + x^3 + 1$. Similar to the case with the finite field GF(2^9), a correspondence between the power and vector representations is established using this primitive polynomial. In this case, the longest symbol length in the RS code is 255 (2^8-1), and $2t$ check symbols are required to achieve error correction of t symbols (i.e., t pillars). However, to align the number of channel bits to be recorded and reproduced for the FER calculated in Figure 6, two RS code blocks made up of 255 symbols are combined to make up 510 pillars to form one frame.

Figure 8 shows the flame error rate (FER) performance for σ_{DW} in the short pillar model. The ●, ●, ●, ● symbols show the FER performances when the correctable t symbols per RS codeword are 4, 8, 12, and 16, respectively. It was found that the decoding can achieve the FER less than 10^{-3} when $\sigma_{DW} \leq 0.052$ for $t = 4$, $\sigma_{DW} \leq 0.059$ for $t = 8$, $\sigma_{DW} \leq 0.063$ for $t = 12$, and $\sigma_{DW} \leq 0.066$ for $t = 16$. Increasing corrected symbol t reduces the coding rate, but it is clarified that the coding rate is tolerant to large σ_{DW}.

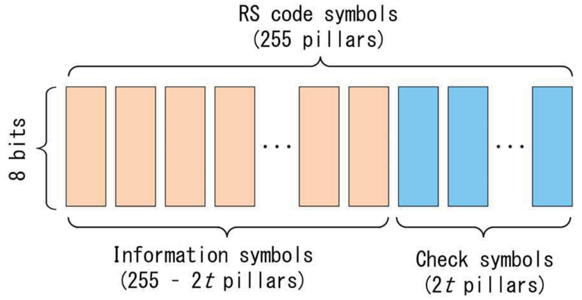

Fig. 7 Codeword structure of RS code for shot pillar model.

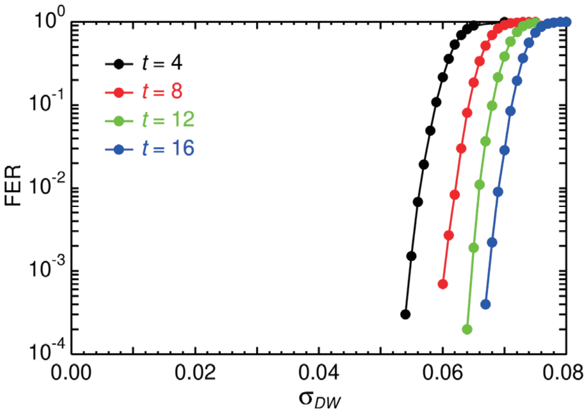

Fig. 8 FER performance for σ_{DW} in short pillar model. Total of 10,000 frames are used.

5. Conclusion

We modeled a read/write channel that exhibits deletion and insertion errors caused by fluctuations in magnetic domain wall displacement in domain wall memory, and investigated methods for correcting these errors. It was clarified that when seven pillars were collectively encoded using an RS code correcting one erroneous pillar in addition to the Levenshtein code, the system tolerated domain wall displacement fluctuations in the range of approximately 0.014 to 0.042. Furthermore, it was clarified that by RS-encoding 255 short pillars, stacking 8 bits, tolerance to displacement fluctuations improved to approximately 0.053 to 0.066.

Acknowledgements This study was supported by CREST, Japan Science and Technology Agency (Grant No. JPMJCR21C1).

References

1) Y. M. Hung, T. Li, R. Hisatomi, Y. Shiota, T. Moriyama, and T. Ono: *J. Magn. Soc. Jpn.*, **45**, 6 (2021).
2) S. Honda and Y. Sonobe: *J. Phys. D: Appl. Phys.*, **57**, 175002 (2024).
3) S. Honda and Y. Sonobe: *J. Phys. D: Appl. Phys.*, **57**, 325002 (2024).
4) V. I. Levenshtein: *Sov. Phys. Dokl.*, **10**, 707 (1966).
5) I. S. Reed and G. Solomon: *J. Soc. Ind. Appl. Math.*, **8**, 300 (1960).
6) A. Goda: *IEEE Trans. Electron Devices*, **67**, 1374 (2020).

Received Apl. 26, 2025; Accepted Jul. 23, 2025

J. Magn. Soc. Jpn., **50**, 6-11 (2026)

<Paper>

Influence of Thermal Gradient and Cooling Rate on Writability in Heat-Assisted Magnetic Recording

T. Kobayashi, Y. Nakatani*, and I. Tagawa**
Graduate School of Engineering, Mie Univ., *1577 Kurimamachiya-cho, Tsu 514-8507, Japan*
*Graduate School of Informatics and Engineering, Univ. of Electro-Communications, *1-5-1 Chofugaoka, Chofu 182-8585, Japan*
**Electrical and Electronic Engineering, Tohoku Institute of Technology, *35-1 Yagiyama-Kasumicho, Sendai 982-8577, Japan*

We analyze the influence of thermal gradient and cooling rate on writability in 4 Tbpsi shingled heat-assisted magnetic recording employing a stochastic calculation. We separate the bit error rate bER for each grain column in 2 bits of data and focus on the mean magnetization reversal number per unit time N_- for the medium in the recording direction during writing. We introduce the medium writing temperature ΔT_{med} and time τ_{med}, which are temperature and time ranges, respectively, where the N_- value is larger than 1 ns^{-1}. We also introduce the Curie temperature variation time τ_{Tc} and the field end temperature T_{end}. The τ_{med} and τ_{Tc} values are functions of the cooling rate, which is the product of the thermal gradient and the linear velocity. In contrast, the T_{end} value is a function of the thermal gradient only. When the writing field is small, write-error and erasure-before-write are mainly dominant, and the bER value is determined by the τ_{med} and τ_{Tc} values, respectively. When the writing field is large, erasure-after-write is mainly dominant, and the bER value is determined by the T_{end} value in addition to the τ_{Tc} value.

Key words: HAMR, stochastic calculation, thermal gradient, cooling rate, linear velocity, medium writing temperature, medium writing time, Curie temperature variation time, field end temperature

1. Introduction

Heat-assisted magnetic recording (HAMR) is a promising candidate as a next generation magnetic recording method in the information explosion era. HAMR is a recording method where the medium is heated to reduce magnetic anisotropy during the writing period. There are many error factors that can affect writability in HAMR media.

Zhu and Li pointed out erasure-after-write (EAW)1) as an error factor employing a micromagnetic simulation. EAW means that when the writing field magnitude is too large, some grain magnetizations are reversed in the opposite direction to the recording direction. This is caused by changing the writing field direction after writing.

Li and Zhu also discussed the impact of Curie temperature T_{c} variation2) on writability employing a micromagnetic simulation.

Akagi *et al.* reported writability in heated-dot magnetic recording (HDMR), namely HAMR on bit patterned media, employing a micromagnetic simulation. They assumed the medium material to be FePt. However, the anisotropy constant K_{u} was smaller3) than that of bulk FePt.

We have previously discussed the error factors4), namely

(1) erasure-before-write (EBW)4),
(2) erasure-after-write (EAW)1),
(3) T_{c} variation2),
(4) write-error (WE),
(5) statistical factor, and
(6) anisotropy constant3),

in relation to writability in HAMR employing a stochastic calculation based on the Néel-Arrhenius model with a Stoner-Wohlfarth dot. EBW means that some grains are magnetized in the opposite direction to the recording direction before changing the writing field direction to the recording direction. We explained the influence of error factors on writability using the mean magnetization reversal number per unit time in our stochastic calculation. A feature of our stochastic calculation is that it is easy to grasp the physical implication of HAMR writing including HDMR.

Writability has already been discussed in terms of thermal gradient and linear velocity1). In this paper, we analyze the influence of

(7) thermal gradient and cooling rate

on writability in 4 Tbpsi shingled HAMR using the mean magnetization reversal number per unit time. The cooling rate $\partial T/\partial t$ is the product of the thermal gradient $\partial T/\partial x$ and the linear velocity v.

2. Calculation Conditions and Method

2.1 Grain arrangement and medium structure

The grain arrangement and medium structure in 4 Tbpsi shingled HAMR4) are shown in Fig. 1. We chose a mean grain size D_{m} of 4.2 nm, a mean grain spacing Δ_{G} of 1.0 nm, and a grain arrangement of 3 (row i) × 2 (column j) = 6 grains/bit. The grain height h was 8.5 nm. The bit length D_{B} and track width D_{T} were 10.4 and 15.6 nm, respectively. The x, y, and z directions were the down-track, cross-track, and film normal, respectively. The 3rd row (i = 3) grains were used as a guard band and the net grain number was 2×2 = 4

Corresponding author: T. Kobayashi (e-mail: kobayasi @phen.mie-u.ac.jp).

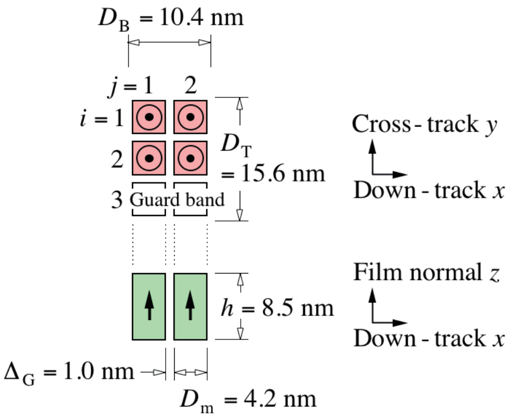

Fig. 1 Grain arrangement and medium structure in 4 Tbpsi shingled HAMR[4].

grains/bit.

We generated the grains D_{ij} with a log-normal size distribution with a standard deviation σ_D. We used a σ_D/D_m value of 15 %.

2.2 Magnetic properties

We used a mean Curie temperature T_{cm} of 750 K and a standard deviation σ_{Tc} of 2 %. The T_c distribution was assumed to be normal.

We used a K_u value of 51 Merg/cm^3 and an anisotropy field H_k of 107 kOe at a readout temperature of 330 K[4].

2.3 Temperature profile and writing field

For the sake of simplicity, we assumed the thermal gradient $\partial T/\partial x$ in the down-track direction to be constant everywhere. We also assumed the writing field H_w to be spatially uniform, the direction to be perpendicular to the medium plane, and the rise time to be zero.

The calculation conditions are summarized in Table 1. The Gilbert damping constant α was 0.1.

2.4 Stochastic calculation method

The information stability for 10 years of archiving has been discussed employing the Néel-Arrhenius model with a Stoner-Wohlfarth grain[5]. During writing in HAMR, the magnetization reversal is the non-Néel-Arrhenius type where $|H_w| > H_k$. However, the duration for the non-Néel-Arrhenius type is very short, and most of the writing time is the Néel-Arrhenius type where $|H_w| < H_k$. Therefore, stochastic magnetization reversal under thermal agitation is dominant even as regards writability.

The mean magnetization reversal number per unit time N is expressed as

$$N = f_\alpha \exp(-K_\beta), \qquad (1)$$

based on the Néel-Arrhenius model with a Stoner-Wohlfarth grain, where f_α is the attempt frequency[6] and K_β is the thermal stability factor. The f_α value gives an attempt number per unit time for magnetization reversal, and the Boltzmann factor $\exp(-K_\beta)$ is interpreted as the probability of magnetization reversal.

Table 1 Calculation conditions

Recording density (Tbpsi)	4
Mean grain size D_m (nm)	4.2
Standard deviation σ_D / D_m (%)	15
Mean grain spacing Δ_G (nm)	1.0
Grain height h (nm)	8.5
Bit length D_B (nm)	10.4
Track width D_T (nm)	15.6
Mean Curie temperature T_{cm} (K)	750
Standard deviation σ_{Tc} / T_{cm} (%)	2
Anisotropy constant K_u (330 K) (Merg/cm^3)	51
Anisotropy field H_k (330 K) (kOe)	107
Gilbert damping constant α	0.1

When the $|H_w|$ value is less than H_k, $f_\alpha \equiv f_{\alpha+}$, $K_\beta \equiv K_{\beta+}$, and $N \equiv N_+$ are given by

$$f_{\alpha+} = \frac{\gamma\alpha}{1+\alpha^2}\sqrt{\frac{M_s H_k^3 V}{2\pi kT}}\left(1-\left(\frac{|H_w|}{H_k}\right)^2\right)\left(1+\frac{|H_w|}{H_k}\right), \qquad (2)$$

$$K_{\beta+} = \frac{K_u V}{kT}\left(1+\frac{|H_w|}{H_k}\right)^2, \text{ and} \qquad (3)$$

$$N_+ = f_{\alpha+} \exp(-K_{\beta+}), \qquad (4)$$

respectively, for magnetization reversal in the opposite direction to the recording direction, where γ, M_s, V, k, and T are the gyromagnetic ratio, magnetization, grain volume $V = D_{ij}^2 \times h$, Boltzmann constant, and temperature, respectively. We used a γ value of 1.76×10^7 rad s^{-1} Oe^{-1}. For magnetization reversal in the recording direction, $f_\alpha \equiv f_{\alpha-}$, $K_\beta \equiv K_{\beta-}$, and $N \equiv N_-$ are given by

$$f_{\alpha-} = \frac{\gamma\alpha}{1+\alpha^2}\sqrt{\frac{M_s H_k^3 V}{2\pi kT}}\left(1-\left(\frac{|H_w|}{H_k}\right)^2\right)\left(1-\frac{|H_w|}{H_k}\right), \qquad (5)$$

$$K_{\beta-} = \frac{K_u V}{kT}\left(1-\frac{|H_w|}{H_k}\right)^2, \text{ and} \qquad (6)$$

$$N_- = f_{\alpha-} \exp(-K_{\beta-}), \qquad (7)$$

respectively.

In our stochastic calculation, we used the effective anisotropy constant K_{ueff} instead of K_u and the effective anisotropy field H_{keff} instead of H_k, taking account of the shape anisotropy[7], as

$$K_{ueff} = K_u + \frac{(4\pi - 3N_z)M_s^2}{4}, \qquad (8)$$

$$N_z = 8 \arctan\left(\frac{D_{ij}^2}{h\sqrt{2D_{ij}^2 + h^2}}\right), \text{ and} \qquad (9)$$

$$H_{\mathrm{keff}} = \frac{2K_{\mathrm{ueff}}}{M_{\mathrm{s}}}. \tag{10}$$

Our aim is to grasp the physical implications for the error factors by using a simplified model rather than to reproduce realistic situations quantitatively. Both the demagnetizing field within each grain and the stray field from surrounding grains act as small perturbations. Moreover, calculating stray field requires considerably large computational resources and long calculation times. Therefore, the stray field was ignored.

Although there is a period during writing where $|H_{\mathrm{w}}| > H_{\mathrm{keff}}$, the duration is relatively short. The factor $\sqrt{M_{\mathrm{s}}H_{\mathrm{k}}^3/T}$ in Eqs. (2) and (5) has a strong impact on the temperature dependence of $f_{\alpha\pm}$, and $(1-(|H_{\mathrm{w}}|/H_{\mathrm{k}})^2)(1 \pm |H_{\mathrm{w}}|/H_{\mathrm{k}})$ is a weakly impacting factor since the H_{k} value is considerably larger than $|H_{\mathrm{w}}|$ for most of the writing time. Although the $\sqrt{M_{\mathrm{s}}H_{\mathrm{k}}^3/T}$ value becomes zero at T_{c}, $(1-(|H_{\mathrm{w}}|/H_{\mathrm{k}})^2)(1 \pm |H_{\mathrm{w}}|/H_{\mathrm{k}})$ reaches zero at a temperature where $H_{\mathrm{k}} = |H_{\mathrm{w}}|$. We employed the Néel-Arrhenius model for the entire writing time. To achieve this, we extended the $f_{\alpha\pm}$ formula to T_{c} as follows

$$f_{\alpha\pm} = \frac{\gamma\alpha}{1+\alpha^2}\sqrt{\frac{M_{\mathrm{s}}H_{\mathrm{keff}}^3 V}{2\pi kT}}\left(1-\left(\frac{|H_{\mathrm{w}}|}{H_{\mathrm{const}}}\right)^2\right)\left(1 \pm \frac{|H_{\mathrm{w}}|}{H_{\mathrm{const}}}\right), \tag{11}$$

so that the $f_{\alpha\pm}$ value became zero at T_{c}. H_{const} in Eq. (11) is a fitting parameter for Eqs. (2) and (5) and we used a H_{const} value of 60 kOe. When $|H_{\mathrm{w}}| > H_{\mathrm{keff}}$, we assumed that

$$\exp(-K_{\beta-}) = 1. \tag{12}$$

The calculation procedure for the $|H_{\mathrm{w}}|$ value dependence of the bit error rate bER, namely writability, is described below. The dot temperature fell with time from T_{c} according to $\partial T/\partial x$ and v. The attempt times were calculated using $f_{\alpha\pm}$. The probabilities $\exp(-K_{\beta\pm})$ were calculated for every attempt time. The magnetization direction was determined by the Monte Carlo method for every attempt time. Our bER depends on the magnetization direction and area of the grains. The calculation has already been reported in detail[8].

The calculation bit number was 10^6. The bER value in this paper is useful only for comparison.

3. Calculation Results

3.1 Thermal gradient at constant linear velocity

Figure 2 shows the $|H_{\mathrm{w}}|$ value dependence of the bER value in 1 bit of data for various $\partial T/\partial x$ values at a constant v value of 10 m/s. A v value of 10 m/s corresponds to a platter radius of about 27 mm at 3600 rpm. When $|H_{\mathrm{w}}| \lesssim$ 10 kOe, the bER value decreases as the $\partial T/\partial x$ value decreases. Therefore, a small $\partial T/\partial x$ value is preferable. In contrast, when $|H_{\mathrm{w}}| \gtrsim$ 15 kOe, the bER value decreases as the $\partial T/\partial x$ value increases. Therefore, a large $\partial T/\partial x$ value is preferable.

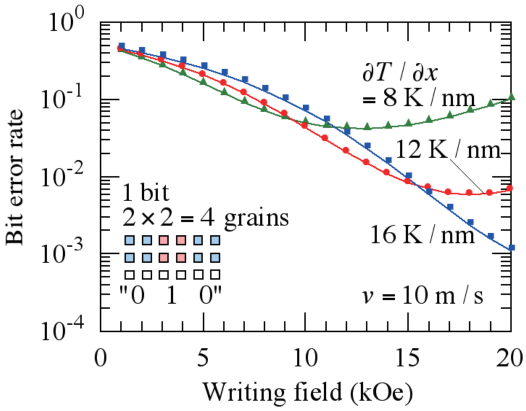

Fig. 2 Writing field $|H_{\mathrm{w}}|$ dependence of bit error rate bER in 1 bit of data for various thermal gradients $\partial T/\partial x$ at a constant linear velocity v of 10 m/s.

There is a trade-off relationship between the bER values for small and large $|H_{\mathrm{w}}|$ values in terms of the $\partial T/\partial x$ value at a constant v value. In the following, we analyze the result in Fig. 2 employing the time dependence of the N_- value in our stochastic calculation.

3.2 Writability parameters

First, we explain the writability parameters we introduced. The medium writing temperature ΔT_{med} and time τ_{med} are the temperature and time ranges determined by the medium during writing, respectively, where the N_- value is larger than 1 ns^{-1}. The value of 1 ns^{-1} is tentative. Since the writing time is of the order of 1 ns, we chose this value as a guideline. We also introduced T_{c} variation time τ_{Tc} and the field end temperature T_{end} at the end of the field writing time, namely the time range determined by the writing field.

The ΔT_{med} value is a function of the $|H_{\mathrm{w}}|$ value, and is independent of $\partial T/\partial x$ and v.

The τ_{med} value is a function of $(\partial T/\partial x) \cdot v$ as,

$$\tau_{\mathrm{med}} = \frac{\Delta T_{\mathrm{med}}}{(\partial T/\partial x) \cdot v}, \tag{13}$$

in which $(\partial T/\partial x) \cdot v$ is a cooling rate $(\partial T/\partial x) \cdot v = (\partial T/\partial x) \cdot (\partial x/\partial t) = \partial T/\partial t$. Write-error (WE) is a normal error where the magnetization does not reverse in the recording direction. WE can be reduced by increasing the ΔT_{med} and τ_{med} values.

The τ_{Tc} value is also a function of $\partial T/\partial t$ as,

$$\tau_{\mathrm{Tc}} = \frac{\sigma_{\mathrm{Tc}}}{(\partial T/\partial x) \cdot v} = \frac{\sigma_{\mathrm{Tc}}}{\partial T/\partial t}. \tag{14}$$

Erasure-before-write (EBW) and erasure-after-write (EAW) are errors where the magnetization reverses in the opposite direction to the recording direction before and after the field writing time, respectively. We have already discussed the influence of the τ_{Tc} value on EBW and EAW[4], and EBW and EAW increase as the τ_{Tc} value increases.

The T_end value is a function of $\partial T/\partial x$ only as,

$$T_\mathrm{end} = T_\mathrm{cm} - (D_\mathrm{m} + \Delta_\mathrm{G})\frac{\partial T}{\partial x}, \tag{15}$$

where $(D_\mathrm{m} + \Delta_\mathrm{G})$ is the grain pitch. EAW increases as the T_end value increases.

3.3 Constant cooling rate (1 bit of data)

Since the $\tau_\mathrm{med} = \Delta T_\mathrm{med}/(\partial T/\partial t)$ value is a function of $\partial T/\partial t$, we calculated the $|H_\mathrm{w}|$ value dependence of the bER value in 1 bit of data for various $\partial T/\partial x$ values at a constant $\partial T/\partial t$ value of 120 K/ns. The result is shown in Fig. 3 (a). The v values were 15, 10, and 7.5 m/s for $\partial T/\partial x$ values of 8, 12, and 16 K/nm, respectively. When $|H_\mathrm{w}| \lesssim$ 10 kOe, the bER values are almost the same regardless of the $\partial T/\partial x$ value. However, when $|H_\mathrm{w}| \gtrsim$ 10 kOe, the bER value decreases as the $\partial T/\partial x$ value increases. Therefore, a large $\partial T/\partial x$ value is preferable as regards the bER. We confirmed the result in Fig. 3 (a) by employing a micromagnetic simulation in which we solved the Landau-Lifshitz-Gilbert (LLG) equation. The LLG calculation method has already been reported in detail[9]. Figure 3 (b) shows the $|H_\mathrm{w}|$ value dependence of the signal to noise ratio SNR calculated employing a micromagnetic simulation where the calculation step time Δt was 0.2 ps. The relationships between the bER and SNR values are shown in Fig. 3 (c). We observe a good correlation between them.

3.4 Constant cooling rate (2 bits of data)

To analyze the bER value in 1 bit of data as shown in Fig. 3 (a), we calculated the bER value using 2 of the 8 grains for each column in 2 bits of data. Figure 4 shows the $|H_\mathrm{w}|$ value dependence of the 2 grain bER value for column numbers j of (a) 1, (b) 2, (c) 3, and (d) 4. The bER for 1 bit of data corresponds to those for j = 1 and 4.

The bER values for j = 1 are the same regardless of the $\partial T/\partial x$ value at a constant $\partial T/\partial t$ value as shown in Fig. 4 (a). Figure 5 shows the $N_- = f_{\alpha-}\exp(-K_{\beta-})$ value as a function of time during writing for j = 1 and $|H_\mathrm{w}|$ = 10 kOe. The grain temperature for j = 1 is also shown. At a time of zero, the grain temperature is T_cm and the H_w direction changes from downward to upward. The τ_med values are the same regardless of the $\partial T/\partial x$ value and the T_c value of (a) T_cm or (b) $T_\mathrm{cm} + \sigma_\mathrm{Tc}$ at a constant $\partial T/\partial t$ value, since $\tau_\mathrm{med} = \Delta T_\mathrm{med}/(\partial T/\partial t)$. The bER value for j = 1 includes EBW in addition to WE. When $T_\mathrm{c} = T_\mathrm{cm} + \sigma_\mathrm{Tc}$, the time for writing is advanced by the τ_Tc value. Since the $\tau_\mathrm{Tc} = \sigma_\mathrm{Tc}/(\partial T/\partial t)$ value is also a function of $\partial T/\partial t$, the τ_Tc values are also the same regardless of the $\partial T/\partial x$ value at a constant $\partial T/\partial t$ value as shown in Fig. 5 (b). Therefore, the bER values for j = 1 are the same regardless of the $\partial T/\partial x$ value as shown in Fig. 4 (a). The bER value for j = 2 in Fig. 4 (b) is smaller than that for j = 1 in Fig. 4 (a), since there is no EBW in Fig. 4 (b).

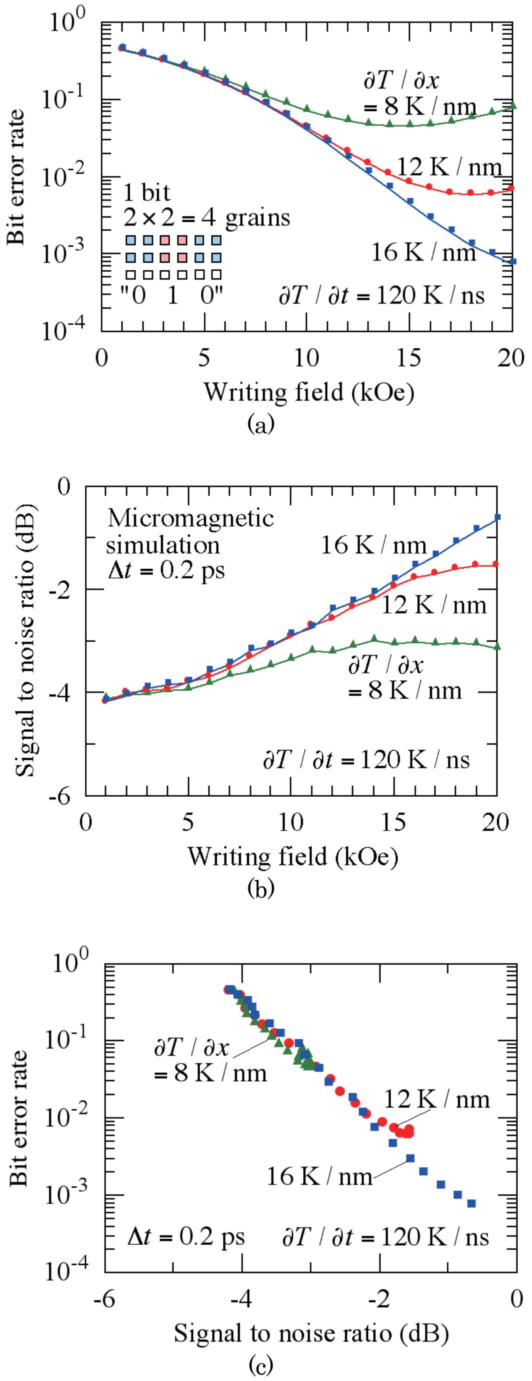

(a)

(b)

(c)

Fig. 3 Writing field $|H_\mathrm{w}|$ dependence of (a) bit error rate bER in 1 bit of data calculated employing our stochastic calculation and (b) signal to noise ratio SNR calculated employing a micromagnetic simulation for various thermal gradients $\partial T/\partial x$ at a constant cooling rate $\partial T/\partial t$ of 120 K/ns. (c) The bER value in (a) as a function of the SNR value in (b).

EAW can be seen in the bER value for j = 3 and $\partial T/\partial x$ = 8 K/nm when $|H_\mathrm{w}| \gtrsim$ 15 kOe as shown in Fig. 4 (c). Furthermore, there is EAW in the bER values for j = 4 and all the $\partial T/\partial x$ values used as shown in Fig.4 (d). Figure 6 shows the $N_- = f_{\alpha-}\exp(-K_{\beta-})$ value as a function of temperature during writing for j = 4 and $|H_\mathrm{w}|$ = 20 kOe. The $T_\mathrm{end} = T_\mathrm{cm} - (D_\mathrm{m} + \Delta_\mathrm{G}) \cdot (\partial T/\partial x)$ value is a function of $\partial T/\partial x$ only. The T_end values are

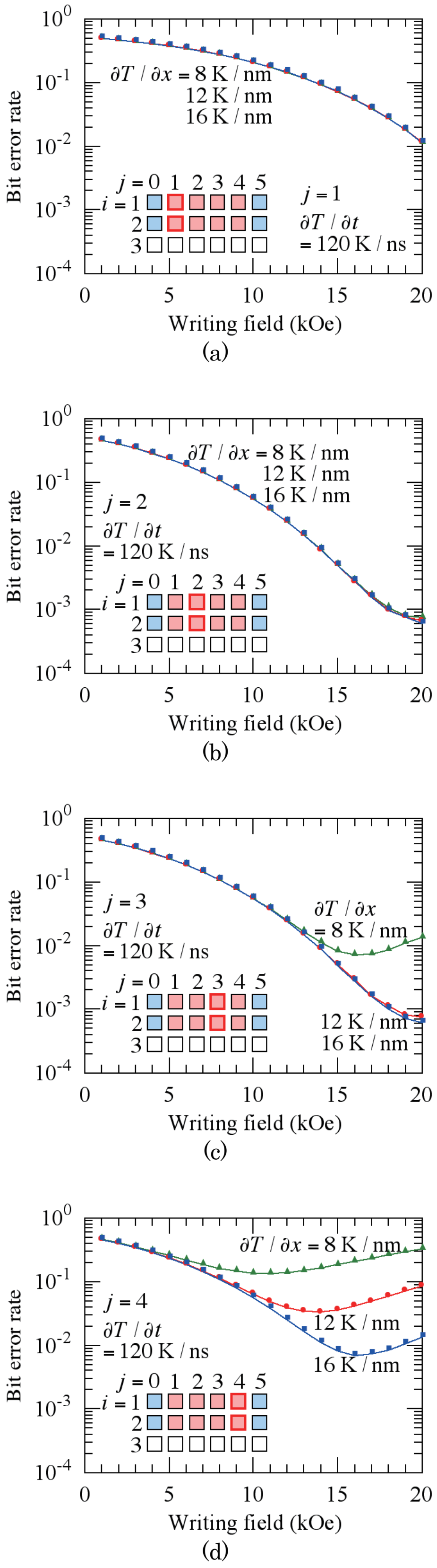

(a)

(b)

(c)

(d)

Fig. 4 Writing field $|H_w|$ dependence of bit error rate bER (2 grains) in 2 bits of data for various thermal gradients $\partial T/\partial x$ at a constant cooling rate $\partial T/\partial t$ of 120 K/ns for each column number j = 1 to 4. (a) j = 1, (b) 2, (c) 3, and (d) 4.

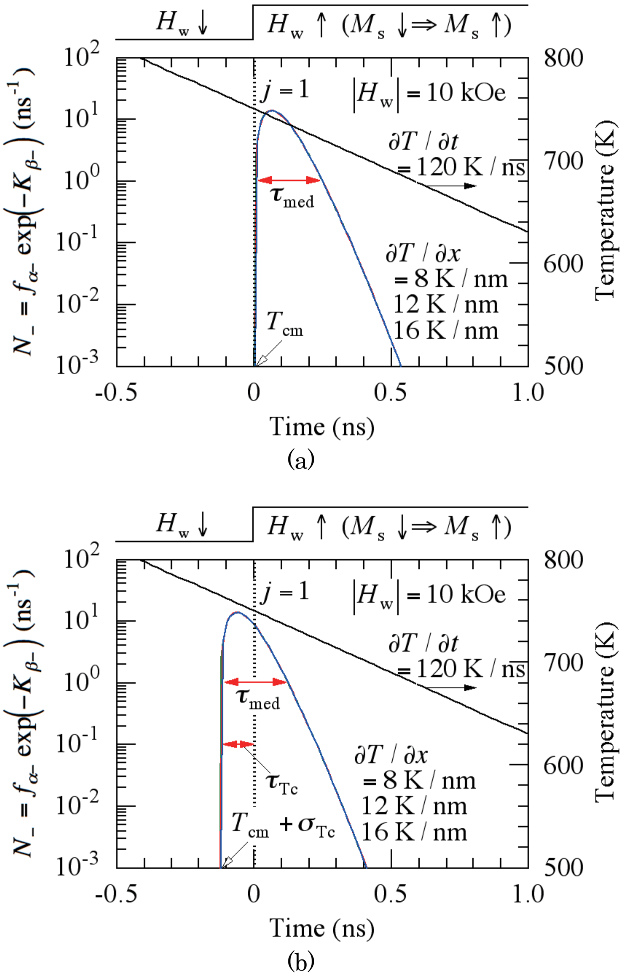

(a)

(b)

Fig. 5 Mean magnetization reversal number per unit time $N_- = f_{\alpha-}\exp(-K_{\beta-})$ as a function of time during writing for Curie temperatures T_c of (a) T_{cm} and (b) $T_{cm} + \sigma_{Tc}$ at a constant cooling rate $\partial T/\partial t$ of 120 K/ns where j = 1 and $|H_w|$ = 10 kOe. Grain temperature for j = 1 is also shown.

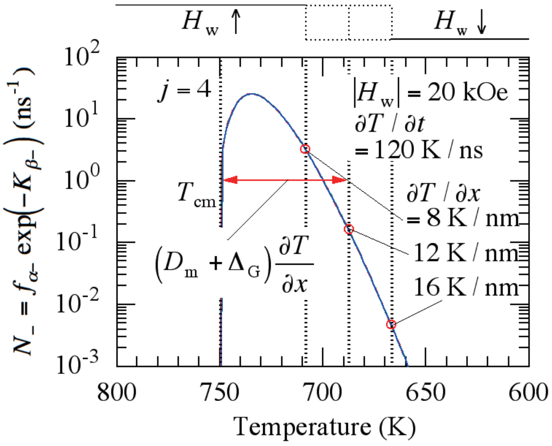

Fig. 6 Mean magnetization reversal number per unit time $N_- = f_{\alpha-}\exp(-K_{\beta-})$ as a function of temperature during writing for various thermal gradients $\partial T/\partial x$ at a constant cooling rate $\partial T/\partial t$ of 120 K/ns where j = 4 and $|H_w|$ = 20 kOe.

667, 688, and 709 K for $\partial T/\partial x$ values of 16, 12, and 8 K/nm, respectively. The N_- value and thus EAW increases as the T_{end} value increases, namely the $\partial T/\partial x$ value decreases. Therefore, the bER value for j = 4 increases as the $\partial T/\partial x$ value decreases as shown in Fig. 4 (d). A large $\partial T/\partial x$ value is preferable for EAW even at a constant $\partial T/\partial t$ value.

3.5 Cooling rate at constant linear velocity (j = 1)

At a constant v value of 10 m/s, the bER value for j = 1 uniformly decreases as the $\partial T/\partial t$ value decreases as shown in Fig. 7 (a). The $\partial T/\partial x$ values were 16, 12, and 8 K/nm for $\partial T/\partial t$ values of 160, 120, and 80 K/ns, respectively. When $T_{\mathrm{c}} = T_{\mathrm{cm}} + \sigma_{\mathrm{Tc}}$, EBW increases as the $\partial T/\partial t$ value decreases, since $\tau_{\mathrm{Tc}} = \sigma_{\mathrm{Tc}}/(\partial T/\partial t)$ increases. However, WE decreases, since $\tau_{\mathrm{med}} = \Delta T_{\mathrm{med}}/(\partial T/\partial t)$ increases as shown in Fig. 7 (b). The τ_{med} value is larger than the τ_{Tc} value at $|H_{\mathrm{w}}|$ = 10 kOe as shown in Fig. 5 (b). Furthermore, half of the grains have a Curie temperature of $T_{\mathrm{c}} < T_{\mathrm{cm}}$. The bER value is independent of EBW for grains with $T_{\mathrm{c}} < T_{\mathrm{cm}}$, since the time for writing is delayed from zero. Therefore, the bER value for j = 1 decreases as $\partial T/\partial t$, namely the $\partial T/\partial x$ value decreases as shown in Fig. 7 (a). A small $\partial T/\partial t$, namely a small $\partial T/\partial x$ value is preferable for WE at a constant v value.

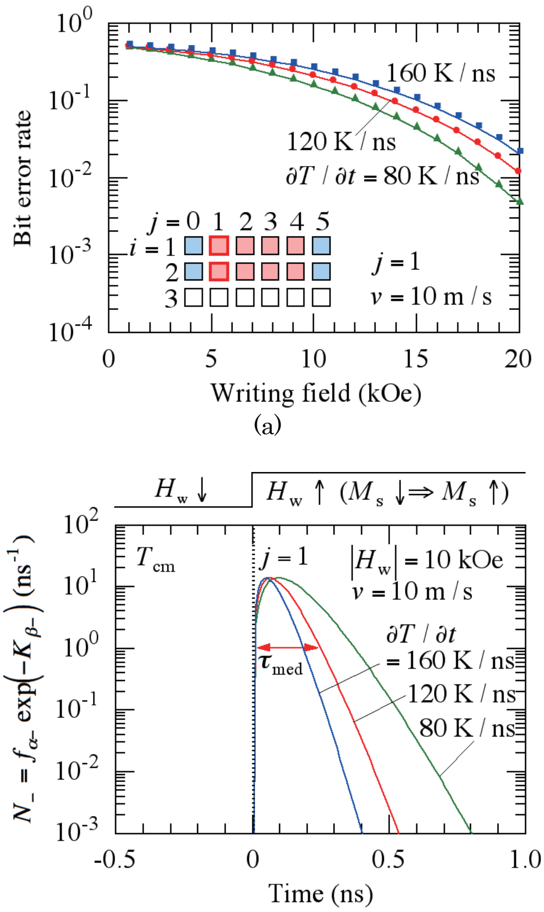

(a)

(b)

Fig. 7 (a) Writing field $|H_{\mathrm{w}}|$ dependence of bit error rate bER (2 grains) in 2 bits of data for various cooling rates $\partial T/\partial t$ at a constant linear velocity v of 10 m/s for j = 1 and (b) mean magnetization reversal number per unit time $N_- = f_{\alpha-}\exp(-K_{\beta-})$ as a function of time during writing where j = 1 and $|H_{\mathrm{w}}|$ = 10 kOe.

As a result, for the bER value in 1 bit of data for various $\partial T/\partial x$ values at a constant v value as shown in Fig. 2, when $|H_{\mathrm{w}}| \lesssim$ 10 kOe, WE and EBW are mainly dominant and affected by the τ_{med} and τ_{Tc} values, respectively. WE and EBW are functions of $\partial T/\partial t$ as shown in Figs. 4 (a) and 7 (a). Therefore, the bER value decreases as the $\partial T/\partial x$ value decreases. When $|H_{\mathrm{w}}| \gtrsim$ 15 kOe, EAW is mainly dominant and affected by the T_{end} value in addition to the τ_{Tc} value. The T_{end} value is a function of $\partial T/\partial x$ as shown in Fig. 6. Therefore, the bER value decreases as the $\partial T/\partial x$ value increases.

4. Conclusions

We analyzed the error factor for writability in HAMR in terms of the thermal gradient $\partial T/\partial x$ and cooling rate $\partial T/\partial t$.

When the writing field is small, write-error and erasure-before-write are mainly dominant and affected by the medium writing time τ_{med} and Curie temperature variation time τ_{Tc}, respectively. The τ_{med} and τ_{Tc} values are functions of $\partial T/\partial t$. When the writing field is large, erasure-after-write is mainly dominant and affected by the field end temperature T_{end} in addition to the τ_{Tc} value. The T_{end} value is a function of $\partial T/\partial x$.

A small $\partial T/\partial t$ value for write-error and a large thermal gradient $\partial T/\partial x$ for erasure-after-write are preferable as regards the bit error rate. Therefore, a large $\partial T/\partial x$ value and a low linear velocity v are necessary for realizing small $\partial T/\partial t = (\partial T/\partial x) \cdot v$ and large $\partial T/\partial x$ values simultaneously.

Acknowledgement We acknowledge the support of the Advanced Storage Research Consortium (ASRC), Japan.

References

1) J. -G. Zhu and H. Li: *IEEE. Trans. Magn.*, **49**, 765 (2013).
2) H. Li and J. -G. Zhu: *J. Appl. Phys.*, **115**, 17B744 (2014).
3) F. Akagi, M. Mukoh, M. Mochizuki, J. Ushiyama, T. Matsumoto, and H. Miyamoto: *J. Magn. Magn. Mater.*, **324**, 309 (2012).
4) T. Kobayashi, I. Tagawa, and Y. Nakatani: *J. Magn. Soc. Jpn.*, **49**, 47 (2025).
5) S. H. Charap, P. -L. Lu, and Y. He: *IEEE Trans. Magn.*, **33**, 978 (1997).
6) E. D. Boerner and H. N. Bertram: *IEEE Trans. Magn.*, **34**, 1678 (1998).
7) T. Kobayashi and I. Tagawa: *J. Magn. Soc. Jpn.*, **47**, 128 (2023).
8) T. Kobayashi, Y. Nakatani, and Y. Fujiwara: *J. Magn. Soc. Jpn.*, **42**, 110 (2018).
9) T. Kobayashi, Y. Nakatani, and Y. Fujiwara: *J. Magn. Soc. Jpn.*, **47**, 1 (2023).

Received Jun. 2, 2025; Revised Jul. 20, 2025; Accepted Nov. 11, 2025

INDEX

J. Magn. Soc. Jpn., **50**, 12-18 (2026)

<Paper>

Fabrication of Magnetizable Concrete for Wireless Power Transfer and Its Properties

Shin Tajima, Norika Miura, Yuko Kano, Koji Shigeuchi, and Shuntaro Inoue
Toyota Central R&D Labs., Inc. *41-1 Yokomichi, Nagakute, Aichi 480-1192, Japan*

Electric vehicles face range limitations, and expanding battery capacity raises cost and environmental concerns. Dynamic wireless power transfer (DWPT) offers a solution by charging electric vehicles while driving, but conventional road materials reduce transmission efficiency. Magnetizable concrete, in which magnetic materials are used as concrete aggregates, was considered to improve the efficiency of power transmission for DWPT. The use of plate-like Mn–Zn ferrite powder (to increase permeability) and Fe–10Si–5Al powder made from a crushed dust core (to reduce eddy current loss) was examined to enhance the properties of magnetizable concrete. In addition, a mixture of magnetic powders with different particle sizes was used as an aggregate to increase the filling rate of the magnetic powders in the concrete. As a result, magnetizable concrete with the following properties was obtained: cement concrete using plate-like Mn–Zn ferrite powder showed a specific permeability of 73 and iron loss (85 kHz and 0.05 T) of 270 kW/m^3; geopolymer concrete using Fe–10Si–5Al powder showed a specific permeability of 21 and iron loss of 300 kW/m^3.

Keyword: Magnetizable concrete, Geopolymer, Cement, Dynamic wireless power transfer, Specific permeability, Iron loss.

1 Introduction

A key issue for electric vehicles, which are one of the means to achieve carbon neutrality, is their shorter cruising range compared with that of vehicles with internal combustion engines. To extend the cruising range, the number of batteries installed should be increased; however, lithium-ion batteries are expensive, and the environmental impact of mining raw materials is problematic.

To solve this problem, a system called dynamic wireless power transfer (DWPT) has been proposed, which minimizes the number of batteries installed in the vehicle and supplies power while the vehicle is running (Fig. 1)[1-5]. Various methods for DWPT have been investigated. In the magnetic coupling type, a coil for wireless power transfer (transmission coil) is embedded in the road, a receiving coil is mounted on the automobile side, and power is supplied during driving through magnetic-field coupling. Demonstration tests are currently being conducted in various countries to confirm the effectiveness of this system.

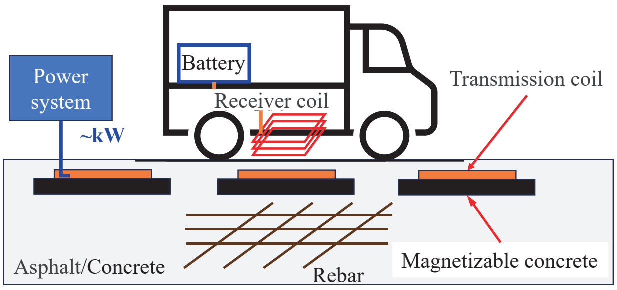

Fig. 1 Schematic diagram of dynamic wireless power transfer (DWPT) for electric vehicles.

There are two main problems with burying transmission coils in roads. First, asphalt and concrete are non-magnetic materials (specific magnetic permeability $\mu_r \approx 1$). In magnetic-field coupling, the transmission efficiency can be improved by concentrating on the magnetic flux as close to the coil as possible. Second, eddy current loss is caused by the surrounding magnetic and metallic materials. In particular, it has been reported that the presence of rebars in concrete roads significantly reduces the power-transmission efficiency[3, 6]. Therefore, it is necessary to place magnetic materials with appropriate magnetic properties between the coil and rebar, as shown in Fig. 1.

Previous studies have addressed this problem by arranging large plate-like sintered bodies of Mn–Zn ferrite ($(Mn,Zn)Fe_2O_4$)[1]. As a result, an improvement in the transmission efficiency has been achieved; however, large Mn–Zn ferrite sintered bodies are expensive, and the installation of sintered bodies on the road incurs additional construction costs. To solve this problem, magnetizable concrete, which utilizes magnetic materials as aggregates, has been considered[6-9]. This material is a type of magnetic composite (dust core), and its properties can be understood by considering composite material science[10-12]. For example, Magment GmbH has presented a magnetizable concrete, "Magment," made by removing sintered Mn–Zn ferrite from discarded electronic equipment and power supplies, crushing it to an appropriate size, and using it as an aggregate[13]. Currently, a large number of ferrite and dust cores are being produced. Therefore, this business model is also valuable from the perspective of the circular economy.

However, magnetizable concrete using Mn–Zn ferrite might pose significant environmental concerns. Mn compounds are specific chemical substances; therefore, the burial of such substances beneath roadways may pose a risk of environmental contamination. In addition, Mn is a type of rare metal, and its extraction has the potential to cause

---

Corr. Author: S. Tajima (e-mail: e0954@mosk.tytlabs.co.jp).

significant environmental damage. Therefore, it is necessary to develop magnetizable concrete using magnetic materials that pose low resource risks and have minimal potential for environmental contamination. In other words, to extend the DWPT system to electric vehicles, the development of magnetizable concrete with minimal environmental impact is essential. For this purpose, the use of magnetizable concrete incorporating the Fe–10Si–5Al alloy as a magnetic material is proposed, as it is not composed of rare metals or environmentally harmful elements.

A brief overview of concrete is provided below[14, 15]. Concrete is made by mixing sand or stone (aggregate) with a binder such as cement and adding water. A typical concrete mix ratio is 30 vol% cement and 70 vol% aggregate. The main compound in cement is Ca_3SiO_5, which hardens via the following hydration reaction (hydraulic hardening):

$$2Ca_3SiO_5 + 6H_2O \rightarrow Ca_3Si_2O_{10}H_6 + 3Ca(OH)_2 \quad (1)$$

All added water reacts with Ca_3SiO_5 and remains in the concrete as a hydrate without evaporating. $Ca_3Si_2O_{10}H_6$ has an amorphous fibrous structure, and the fibrous material intertwines and hardens. The produced $Ca(OH)_2$ makes the concrete alkaline, which prevents corrosion of the rebar in the concrete. The cement does not react with the aggregates.

Ca_3SiO_5 is produced from limestone ($CaCO_3$) and silica sand (SiO_2):

$$3CaCO_3 + SiO_2 \rightarrow Ca_3SiO_5 + 3CO_2\uparrow \quad (2)$$

The reaction is conducted at a high temperature (~1450 °C). Even if the energy required for this process is entirely renewable, it inherently emits large amounts of CO_2. Therefore, geopolymers have recently been investigated as alternatives to cement binders. Geopolymers were initially developed by Davidovits in France in the 1970s and are defined as "a raw material (active filler) consisting mainly of amorphous aluminum silicate, without cement, hardened with alkali metal silicates and alkali stimulants (alkali metal carbonates and hydroxides)”[16-19]. Because of their raw material composition, they are expected to be CO_2-free. However, their production remains limited because they are slightly more expensive than cement and less convenient to use.

The purpose of this study is to investigate magnetizable concrete suitable for DWPT systems. Several detailed reports exist on the relationship among mixing ratios, manufacturing conditions, strength, and magnetic properties of magnetizable concrete; however, many aspects of the material remain unknown[6, 7, 9, 20, 21]. This study investigates the fabrication of magnetizable concrete using Mn–Zn ferrite and Fe–10Si–5Al-alloy powders and evaluates their basic properties. The important properties of magnetizable concrete are as follows: (1) strength suitable for road applications, (2) permeability to control the magnetic flux and improve the transmission efficiency, and (3) low iron loss in AC magnetic fields. The tentative target properties due to previous studies[6, 20] are as follows: the bending strength ≧ 5 MPa, the maximum specific permeability (μ_m) ≧ 10 and the iron loss (P_c) [kW/m^3] ≦ 600 (frequency of 85 kHz and maximum magnetic flux density (B_m) of 0.05 T). In addition, geopolymer-based magnetizable concrete is also investigated, considering that it is CO_2-free during manufacturing.

2 Experimental

In our previous study, we evaluated small test pieces (*e.g.* φ46 – t6 mm) for this basic investigation[21]. In this study, to improve the properties of magnetizable concrete, specimens of larger size (approximately φ100 – t20 mm) were fabricated and evaluated. There were two reasons for this approach. First, we investigated the effect of particle size distribution. Generally, aggregates of several millimeters in size are used in concrete; however, large aggregates cannot be used in small specimens. Second, we aimed to improve the filling rate of the magnetic powder. For the concrete construction, a large vibrator was used to enhance the filling rate of the aggregates, and this vibrator could be used with the standard mold for concrete test pieces (φ100 mm). However, evaluating the magnetic properties of large magnetic materials was difficult because of their high impedance. To address this, a thin toroidal core (φ100 mm – φ80 mm, t7 mm) was fabricated from the large disk-shaped concrete (approximately φ100 mm – t20 mm) to reduce the impedance of the toroidal core.

2.1 Synthesis of Magnetizable Concrete

2.1.1 Magnetizable Cement Concrete

Commercially available ordinary Portland cement (density: 3.15 Mg/m^3), magnetic powder, and ion-exchanged water were used as raw materials. Magnetic powder was used as an aggregate, and common aggregates such as sand and stone were not included. Mn–Zn ferrite ($(Mn\text{–}Zn)Fe_2O_4$, density: 4.90 Mg/m^3) and Fe–10Si–5Al (density: 6.90 Mg/m^3) powders with the so-called Sendust composition were selected as magnetic powders[22]. Mn–Zn ferrite has a high magnetic permeability and low eddy current loss. On the other hand, the Fe–10Si–5Al powder has an extremely high permeability and high saturation magnetic flux density; however, as a metallic material, it has a high electrical conductivity and eddy current loss[22]. In addition, there are concerns about corrosion during long-term use. According to a previous report, the loss associated with magnetizable concrete using Fe–10Si–5Al powder was too great for use in DWPT[21]. To decrease this loss, crushed powder of the Fe–10Si–5Al dust core was used in this study, in which the surface of each magnetic particle was coated with an insulator, thereby reducing the eddy current loss.

The details of the magnetic powder used are as follows. Ferrite powder (PC95; core material for transformers; TDK Corp., Tokyo, Japan) was used in two forms. The first was a plate-like ferrite sintered body measuring 15 mm × 12 mm × 1.5 mm (hereinafter abbreviated as “plate ferrite”), which was used as an aggregate without being crushed. The second was a crushed powder of Mn–Zn ferrite-sintered bodies which was classified by sieving. These powders were hereinafter referred to as “coarse” (2–6 mm) and “fine” (≦ 2 mm) ferrite powders. The particle size distribution was not measured.

Fe–10Si–5Al powder was also used in two forms. The first was a crushed powder of the Fe–10Si–5Al dust core (MAGPROST Corp., Saitama, Japan, density: 5.90 Mg/m^3), which was similarly classified by sieving into 2 mm or more and 2 mm or less, and hereinafter referred to as "coarse" (2–6 mm) and "fine" (≦ 2 mm) Fe–Si–Al powders, respectively. The particle size distribution was not measured. The second was gas-atomized Fe–10Si–5Al powder (Sanyo Special Steel Co., Ltd., Hyogo, Japan), which was used without further processing. The particles were not coated with insulators, and the mean particle size was 50 µm.

The mixing ratios of each sample are listed in Table 1. All magnetic powders were used in a dry state. The volume fraction of the magnetic powder (V_M) was estimated based on the assumptions that the added water was fully retained and that there was no porosity. Based on our previous report[21)], mixing ratios were selected to enable the highest possible filling rate of the magnetic powder while achieving a high four-point bending strength (≧ 5 MPa). A predetermined amount of the materials was weighed into a stainless-steel beaker, stirred using laboratory spatula by hand for 5 min, and the uniformity of the mixture was checked by visual inspection. The resulting slurry was cast into a cylindrical mold with a diameter of φ100 mm. The mold was placed in a vibration compactor commonly used in concrete fabrication, and the slurry was cast uniformly to ensure proper consolidation. The specimens were sealed to prevent drying, cured for 1 week, and then demolded. The size of the obtained disc specimen was φ100 mm – t20 mm. The demolded specimens were cured at room temperature and humidity for 28 d or longer before evaluation.

2.1.2 Magnetizable Geopolymer Concrete

The raw materials used were geopolymers (comprising an active filler and alkali stimulant), magnetic powder, and ion-exchanged water. The magnetic powder used was the same as that employed in the magnetizable cement concrete, as described in Section 2.1.1. To prepare the geopolymers, the following raw materials were used. As active fillers, either metakaolin (SK Mineral Co., Ltd., Aichi, Japan; calcined and dehydrated clay mineral kaolinite, $Al_4Si_4O_{10}(OH)_{18}$) or mixtures of amorphous SiO_2 (SO-C5, Admatechs Company Ltd., Aichi, Japan) and $Al(OH)_3$ (FUJIFILM Wako Pure Chemical Corp., Osaka, Japan) were utilized [21)]. As alkali stimulants, either water glass, which was prepared by mixing JIS 1st class water glass (FUJIFILM Wako Pure Chemical Corp., Osaka, Japan) at 138 g with 86 g of ion-exchanged water, and a NaOH aqueous solution (38 mass%, NaOH: FUJIFILM Wako Pure Chemical Corp., Osaka, Japan) were used.

The mixing ratios of each sample are listed in Table 1. Since the extent of the dehydration reaction during geopolymer formation is unknown, the V_M was calculated under the assumption that the water in the water glass and NaOH solution remained, while the added water was removed. Porosity was assumed to be zero. Based on previous reports[17, 21, 23-26)], mixing ratios were selected to enable the highest possible filling rate of the magnetic powder while achieving a high four-point bending strength (≧ 5 MPa).

The slurry preparation and casting procedures were the same as those described in Section 2.1.1. The specimens were sealed to prevent drying, cured at 60 °C for 20 h in an oven. After this initial curing, the demolded geopolymer was further cured by drying at 60 °C for 20 h in the oven and then stored at room temperature in air for at least 28 d.

2.2 Characteristics

All samples were prepared with n = 1, and variations such as statistical dispersion were not evaluated. Generally, the property variation of low-permeability soft magnetic materials would be relatively insensitive to changes in process or conditions.

The structure of the magnetizable concrete was observed both visually and using an optical microscope.

The magnetic properties of the resulting magnetizable concrete were also evaluated. The surface of the specimens was polished, and the interior was hollowed out to form a ring shape (φ100 mm – φ80 mm, t7 mm). Magnetic properties were measured using a B-H analyzer (SY8218, Iwatsu Electric Co., Ltd., Tokyo, Japan) with toroidal core samples. All measurements were performed at room temperature under conditions of a frequency range of 60–100 kHz and maximum flux density of 0.03–0.05 T. This frequency range was selected because the frequency used in DWPT systems in Japan is 85 kHz. The measurement error was approximately 10%.

3 Results and Discussion

3.1 Structure of Magnetizable Concrete

Fig. 2 shows photographs of the obtained magnetizable concrete. The disk was hollowed out, and the toroidal core was wrapped with a copper wire for magnetic measurements. Plate-shaped ferrites and coarse Fe–Si–Al powders were observed on the surfaces of the discs. The filling rate of the magnetic powder was lower than that of a typical dust core, resulting in numerous gaps between the magnetic particles.

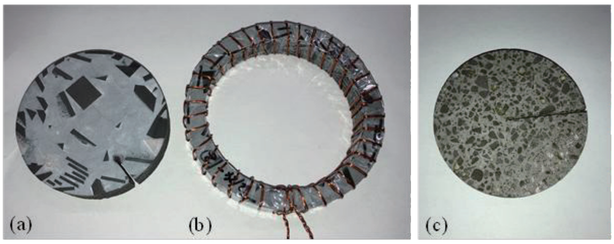

Fig. 2 Photographs of magnetizable concrete. (a) Cem_F_1 from Table 1 (plate-shaped Mn–Zn ferrite sintered body is visible), (b) toroidal coil of Cem_F_1, (c) Geo_S_1 from Table 1 (coarse Fe–Si–Al powder from a crushed Fe–Si–Al dust core is visible).

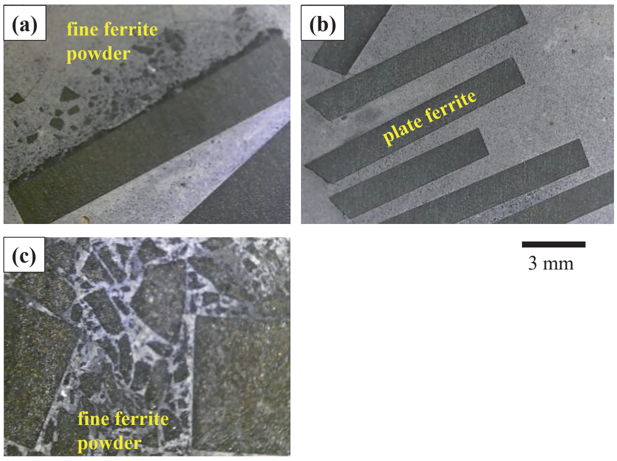

Fig. 3 Structure of magnetizable concrete Cem_F_1 from Table 1.

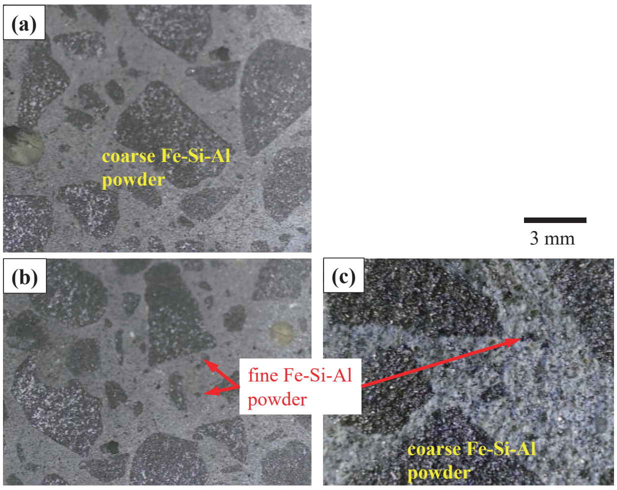

Fig. 4 Structure of magnetizable concrete Geo_S_1 from Table 1.

Table 1 Preparation conditions and characteristics of magnetizable concrete.

Sample No.	Cement / AF [g]	Water [g]	Alkaline for Geopolymer		Magnetic Powder			Curing Condition	Magnetic Properties	
			WG [g]	NaOH [g]	Material Type	[g]	V_M [vol%]		μ_m	Pc [kW/m^3] (= P_h + P_e) 0.05 T, 85 kHz
Cem_F_0	cement 13	8.2	–	–	fine ferrite powder	85	61	RT, 100%HR, 1week	17	430 (= 340+100)
Geo_S_0	metakaolin 15	3	7.5	1.5	Fe-Si-Al atomized powder	85	55	60°C, 100%HR, 20h ⇒60°C, air, 20h	6	600 (=60+540)
Cem_F_1	cement 45	25	–	–	plate ferrite fine ferrite powder	250 200	70	RT, 100%HR, 1week	73	270 (=160+110)
Cem_F_2	cement 45	25	–	–	coarse ferrite powder fine ferrite powder	250 200	70	RT, 100%HR, 1week	51	300 (=180+120)
Geo_F_1	SiO_2+$Al(OH)_3$ 30+10	0	25	5	coarse ferrite powder fine ferrite powder	250 200	71	60°C, 100%HR, 20h ⇒60°C, air, 20h	41	340 (=200+140)
Cem_S_1	cement 45	33	–	–	coarse Fe-Si-Al powder fine Fe-Si-Al powder	280 280	72	RT, 100%HR, 1week	15	350 (=240+110)
Geo_S_1	metakaolin 40	10	25	5	coarse Fe-Si-Al powder fine Fe-Si-Al powder	280 280	72	60°C, 100%HR, 20h ⇒60°C, air, 20h	21	300 (=200+100)
Geo_S_2	metakaolin 40	10	25	5	coarse Fe-Si-Al powder fine Fe-Si-Al powder	310 250	72	60°C, 100%HR, 20h ⇒60°C, air, 20h	15	350 (=240+110)
Geo_S_3	metakaolin 40	10	25	5	coarse Fe-Si-Al powder fine Fe-Si-Al powder	250 310	72	60°C, 100%HR, 20h ⇒60°C, air, 20h	15	350 (=240+110)
Ferrite sintered body									3000	25 (=5+20)
Sendust dust core									129	135 (=67+68)

Top two rows show properties of magnetizable concrete from previous paper[21], while bottom two rows present properties of raw magnetic materials. AF: active filler.

Fig. 3 and Fig. 4 show photographs of the structure of the magnetizable concrete. Fine powder was observed between the ferrite plate and coarse powder on the side of the disk. This occurred because the magnetic powder, being denser than the cement and geopolymer, settled toward the bottom; this phenomenon is commonly observed in concrete. In this study, as the coil is uniformly wound around the entire sample, the measured characteristics reflect the overall average.

The effect of the local inhomogeneity on the magnetic properties is important information, however, a method for measuring the localized magnetic properties inside a magnetic material has not yet been established. In addition, it is also difficult to estimate the effect of the local inhomogeneity using the simulation because the mesh generation is extremely complex and the computation time becomes long. Accordingly, we would like to leave this issue for future investigation.

3.2 Magnetic Properties of the Ferrite Powder System

Table 1 shows the property values of the obtained magnetizable concrete. The maximum specific permeability at 85 kHz is denoted as μ_m [dimensionless], and the iron loss (P_c) [kW/m^3] is measured at a frequency of 85 kHz and maximum magnetic flux density (B_m) of 0.05 T.

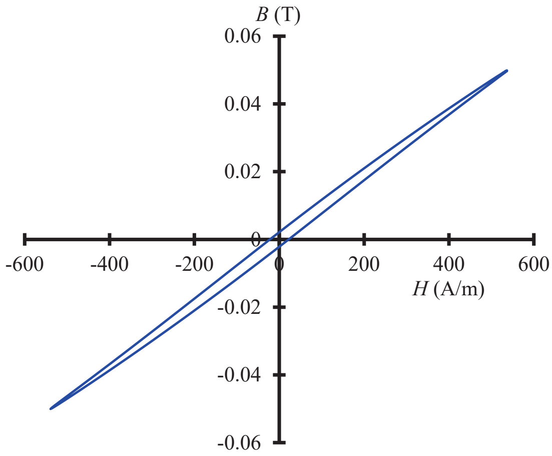

Fig. 5 Typical magnetization curve at f = 85 kHz of magnetizable concrete (Cem_F_1 at Table 1).

Table 2 Frequency and B_m characteristics of P_c at Cem_F_1.

	P_c [kW/m^3]			
	Frequency			
B_m	100 kHz	85 kHz	70 kHz	60 kHz
0.03 T	122	96	72	58
0.04 T	228	179	135	108
0.05 T	345	270	210	170

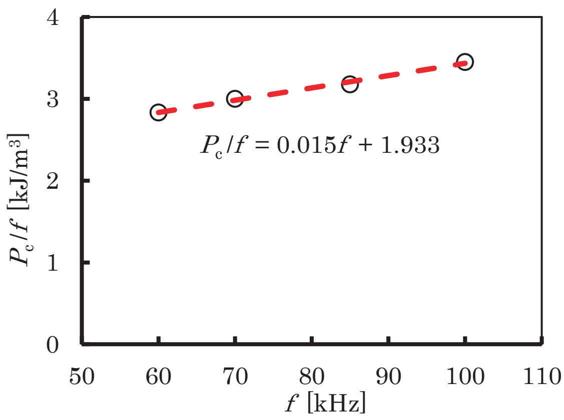

Fig. 6 Frequency (f) characteristics of P_c at Cem_F_1 using Eq. (3) (B_m = 0.05 T).

Fig. 5 shows a typical magnetization curve of the magnetizable concrete (Cem_F_1). The magnetic materials would be used within the range that is not magnetically saturated, as the B_m in the materials was less than 0.07 T according to preliminary electromagnetic simulations[6].

Table 2 and Fig. 6 show the frequency and B_m characteristics of P_c at the representative magnetizable concrete (Cem_F_1). For an AC magnetic field, the P_c is given by Eq. (3), where the residual loss (abnormal eddy current loss) is neglected:

$$P_c = P_h + P_e = K_h \cdot B_m^{1.6} \cdot f + K_e \cdot B_m^2 \cdot f^2 \qquad (3)$$

where P_h is the hysteresis loss, P_e is the eddy current loss, f is the frequency of the AC magnetic field, B_m is the maximum flux density, K_h and K_e are constants, 1.6 is the Steinmetz constant. The Eq. (3) can be used to separate the P_h and P_e as shown in Fig. 6. The division of P_h and P_e at other magnetizable concretes were also revealed at Table 1. As a result, no abnormal eddy current losses were observed in these material systems.

Based on electromagnetic simulation results, provisional target values for the magnetic properties were set as $\mu_m \geqq 10$ and $P_c \leqq 600$ kW/m^3 [6]. The value of μ_m represents the minimum required to control the magnetic flux, while a P_c exceeding the target would significantly reduce the power transmission efficiency. For reference, the magnetic properties of small samples reported in a previous paper are also listed in Table 1 (Cem_F_0 and Geo_S_0)[21]. The target bending strength was set at ≧5 MPa, following the JIS A 5308 standard for roads. Although the strength of the specimens was not evaluated in this study, previous results[21] indicated that these materials were capable of meeting the target.

The properties of magnetizable concrete containing ferrite powder are listed in Table 1 (Cem_F_1 and 2). When plate ferrite powder was used (Cem_F_1), the μ_m was more than three times higher than that of Cem_F_0. There are two reasons for this finding. First, the filling rate of the magnetic powder increased owing to the use of a large mold and powerful vibrator during concrete casting. In the case of transport properties such as permeability and conductivity, the property P_B of a composite material in which particles (magnetic material, in this case) are dispersed in a base material (cement) is expressed as follows[27]:

$$P_B = P_m(P_P+2P_m-2V_M(P_m-P_P))/(P_P+2P_m+V_M(P_m-P_P)) \qquad (4)$$

where P_P is the transport property of the dispersed particles, P_m is the transport property of the matrix, and V_M is the volume fraction (0–1) of the dispersed (magnetic) particles. It is assumed that the particles are spherical (with possible size distribution) and that there is no direct contact between them. According to Eq. (4), the P_B decreases rapidly as the V_M becomes slightly less than 1. This explains why the μ_m of the magnetizable concrete was only several tens, despite the intrinsic μ_m of Mn–Zn ferrite being several thousands.

Next, the shape and orientation of the plate ferrite powder reduced the demagnetizing field, resulting in an improvement in the μ_m. This effect was confirmed by comparing the magnetic properties of Cem_F_1 and Cem_F_2. The μ_m of Cem_F_2, which used the crushed powder, was lower than that of Cem_F_1, despite having the same mixture ratio.

The P_c of Cem_F_1 decreased to 270 kW/m^3 compared with that of the small test piece (Cem_F_0)[21] (P_h = 160 and P_e = 110 kW/m^3 from Eq. (3) and Fig. 6). However, the P_c of the specimens was more than 10 times larger than those of the Mn–Zn ferrite sintered bodies, whose P_c, P_h, and P_e values are 25, 5, and 20 kW/m^3 (at 0.05 T and 85 kHz, room temperature), respectively. The reasons for this increase are discussed below.

The primary cause of the significant increase in the P_c of magnetizable concrete is the effect of the filling rate of the magnetic powder, V_M. In magnetizable concrete, most of the magnetic flux passes through the magnetic material rather than through the cement or geopolymer. Therefore, when the V_M is 50%, the amount of magnetic flux passing through the magnetic material is approximately twice as large. As a result, the P_h increases by approximately $2^{1.6} \approx 3$ times, and the P_e increases by $2^2 \approx 4$ times, according to Eq. (3). In addition, magnetic interactions between magnetic particles related to the V_M were known in dust cores[11], where the P_h decreased as the V_M increased. However, these effects alone could not fully explain the significant increase in the P_c observed in magnetizable concrete.

The second cause is the grinding of the sintered ferrite[20, 28]. When sintered ferrite was pulverized, the P_h was thought to increase owing to the effect of the pulverization strain and pinning effect of the magnetic wall caused by the increase in the specific surface area[29]. However, no quantitative data was obtained in this study. This effect partially explained the increase in the P_h; however, it did not explain the increase in the P_e.

The third is the magnetostrictive effect of the hydrostatic pressure. The aggregate in concrete is subjected to hydrostatic pressure because the cement shrinks slightly as it hardens. This pressure is said to be approximately a few MPa[15, 30]. Several reports discussed the effect of hydrostatic pressure on the magnetic properties of magnetic materials[31-33]. According to these reports, the P_c increased 3–4 times at 100 MPa in the case of Mn–Zn ferrite. It has also been reported that the P_c increased by a factor of 1.5–2 when the toroidal core of Mn–Zn ferrite sintered bodies was embedded in cement[31]. Note that these reports showed an increase in the P_c, but the proportions of the increases in the P_h and the P_e were unknown.

These three factors were assumed to be responsible for the significant increase in the P_c. However, whether these effects were synergistic or harmonious remained unclear. In addition, it was necessary to clarify the proportions of the P_h and P_e that contributed to the increase in the P_c. This investigation will be the subject of our future research.

Geo_F_1 in Table 1 lists the properties of magnetizable concrete using ferrite powder as the magnetic powder and $SiO_2/Al(OH)_3$ as the active filler. According to our previous report [21], the bending strength was approximately 20 MPa, which was more than twice that of magnetizable cement concrete using ferrite powder. The P_c was larger and the μ_m was smaller than those of Cem_F_2, although both used the same ferrite powder. However, the reasons for this trend remain unclear. One possible reason is that, unlike cement, geopolymers could undergo a dehydration reaction during setting, which could result in greater shrinkage compared with cement. As a result, the magnetostrictive effect caused by the stress from this shrinkage could be greater than that in cementitious systems. Therefore, it is possible that the magnetostrictive effect further deteriorates the magnetic properties of geopolymer magnetizable concrete.

3.3 Magnetic Properties of the Fe–Si–Al Powder System

In our previous report[21], the P_c of magnetizable concrete using Fe–Si–Al gas-atomized powder without an insulator on the surface was extremely large owing to the large P_e. For example, 90% of the P_c of the magnetizable concrete was the P_e (P_h = 60 kW/m^3, P_e = 540 kW/m^3). The effect of the insulator on the particle surface on the P_e can be explained as follows. The P_e can be expressed by Eq. (5):

$$P_e \propto B_m{}^2 \cdot f^2 \cdot d^2 / \rho \qquad (5)$$

where B_m is the maximum flux density, f is the frequency, d is the thickness of the sample, and ρ is the electrical resistivity of the sample. For a magnetic core, d in Eq. (5) refers to (1) the diameter of the metallic magnetic particles (primary particle diameter) when they are completely isolated and not in contact with each other, or (2) the particle diameter of the aggregate (secondary particle diameter) when the metallic magnetic particles are in contact with each other and form an aggregate. When aggregates of Fe–Si–Al particles without an insulator are formed, the d increases, and the P_e increases according to Eq. (5). Therefore, a powder made by crushing the Fe–Si–Al dust core (magnetic composite) was used in this study because the surface of the particles was coated with an insulator to reduce the P_e.

As a result, the P_c of all magnetizable concretes using the powder of the Fe–Si–Al dust core (from Cem_S_1 to Geo_S_3 in Table 1) decreased compared with that of the Fe–Si–Al gas-atomized powder. For Geo_S_1, the P_c was 300 kW/m^3 (P_h = 200 kW/m^3, P_e = 100 kW/m^3). However, the P_c was approximately twice as large as that of the Fe–Si–Al dust core used as the raw material, which was 135 kW/m^3 (P_h = 67 kW/m^3, P_e = 68 kW/m^3). The twofold increase in the P_c could be explained by the effect of the magnetic powder filling rate, as described in Eq. (3). This result suggests that the Fe–Si–Al powder had an advantage over the ferrite powder because there was no increase in the P_c due to the magnetostrictive effect under hydrostatic pressure, as previously reported[31, 32].

The μ_m of the magnetizable concrete using Fe–Si–Al powder was lower than that of the magnetizable concrete using the ferrite powder. Although the μ_m (> 10,000) of Fe–Si–Al was larger than that of the Mn–Zn ferrite-sintered body (~3000), the μ_m of the Fe–Si–Al dust core was approximately 120. This is because the density of the dust core was low (relative density ≈ 85%), resulting in a lower μ_m for the magnetizable concrete using the Fe–Si–Al powder compared with that using the Mn–Zn ferrite powder.

The use of a mixture of coarse and fine powders improved the properties of magnetizable concrete, as shown in our previous report[21]. The V_M could be increased by mixing magnetic powders with different particle sizes because fine particles could infiltrate and fill the interstitial spaces among coarse particles. As previously discussed in Eqs. (3) and (4), the magnetic properties could be improved by increasing the V_M. The properties of the magnetizable concrete fabricated by controlling the particle size distribution are shown from Geo_S_1 to Geo_S_3 in Table 1.

This result suggests that the Geo_S_1 ratio yielded the most favorable properties.

4 Conclusion

The preparation and basic properties of magnetizable concrete using magnetic materials as aggregates were investigated. In the case of magnetizable concrete using plate ferrite powder, its magnetic properties were μ_{m} = 73 and P_{c} = 270 kW/m^3. The P_{c} increased significantly compared with that of the ferrite sintered body because of the effect of the filling rate of the magnetic powder, grinding of the sintered ferrite, and magnetostrictive effect under hydrostatic pressure.

Magnetizable concrete using an Fe–Si–Al powder from a crushed dust core with an insulator was fabricated under general conditions. The μ_{m} was 21; however, this value was lower than that of magnetizable concrete using plate ferrite powder. The P_{c} was 300 kW/m^3. The properties were improved compared with those of magnetizable concrete using Fe–S–Al gas-atomized powder without an insulator because the P_{e} was reduced owing to the insulator on the surface of the Fe–Si–Al particles. The degree of increase in the P_{c} indicated that the Fe–Si–Al powder exhibited no magnetostrictive effect under hydrostatic pressure, which was advantageous compared with the ferrite powder. The use of a mixture of coarse and fine powders could improve the properties of magnetizable concrete owing to the increase in the filling rate of the magnetic powder. In addition, the fact that Fe-S-Al does not contain environmentally hazardous elements is an important factor for the widespread adoption of the DWPT system. When installing equipment on roads, there is a possibility that substances within the concrete may spread into the environment during maintenance or excavation work.

We are investigating prototype fabrication and the evaluation of 1/5 a small-scale model of DWPT using the magnetizable concrete. Based on these results, we plan to conduct a detailed full-scale simulation to clarify the effectiveness of the magnetic concrete and to identify the accurate target values.

Acknowledgment We appreciate Mr. Ohtsubo for his assistance with the magnetic property measurements. We also thank Mr. Okuyama for his contribution to the concrete fabrication.

We would like to thank Editage (www.editage.com) for English-language editing.

References

1) K. Matsuo, T. Imura, Y. Hori, M. Kunigo, D. Chimura, S. Shimizu, T. Taniguchi and S. Fujihara: 2024 IEEE Wireless Power Technology Conference and Expo, Kyoto, Japan, (2024).

2) R. Qin, J. Li and D. Costinett: *IEEE Trans. Power Electro.,* **37**, 4842 (2022).

3) K. Matsuo, T. Imura, Y. Hori, M. Kunigo, S. Shimizu and S. Maki: 2023 IEEE Wireless Power Technology Conference and Expo, San Diego, U.S.A., (2023).

4) R. Tavakoli, U. Pratik, E. M. Dede, C. Chou and Z. Pantic: 2021 IEEE Applied Power Electronics Conference and Exposition, (2021).

5) T. Gardner: Wireless Power Transfer Roadway Integration. Utah State University, 2017.

6) S. Inoue, Y. Kano and S. Tajima: 2025 IEEE Applied Power Electronics Conference and Exposition, Atlanta, USA, (2025).

7) C. Carretero, I. Lope and J. Acero: *IEEE J. Emerg. Sel. Top. Power Electron.,* **8**, 2696 (2020).

8) K. A. T. Edwards, S. H. Al-Abed, S. Hosseini and N. A. Brake: *Constr. Build. Mater.,* **227**, 117041 (2019).

9) R. Tavakoli, A. Echols, U. Pratik, Z. Pantic, F. Pozo, A. Malakooti and M. Maguire: *IEEE Xplore,* 4041 (2020).

10) S. Tajima: Magnetic Composite, Corona Publishing Co., Ltd., (2023)

11) S. Tajima, T. Hattori, M. Kondoh, M. Sugiyama, K. Higashiyama, H. Kishimoto and T. Kikko: *Mater. Trans.,* **45**, 1891 (2004).

12) S. Tajima, T. Hattori, M. Kondoh, H. Kishimoto, M. Sugiyama and T. Kikko: *IEEE Trans. Magn.,* **41**, 3280 (2005).

13) Magment GmbH: Dynamic Wireless Charging: https://www.magment.co/ (Date of access：2025/08/25)

14) Y. Arai: Cement no Zairyoukagaku, Dainippon tosho Co.,Ltd., (2021)

15) Y. Fukaya and N. Tuyuki: Cement Concrete Zairyoukagaku, Gizyutsusyoin, (2003)

16) J. Davidovits: *J. Therm. Anal. Calorim.,* **37**, 1633 (1991).

17) K. Harada, K. Ichimiya, J. Tsugo and K. Ikeda: *Proc. Jpn. Concr. Inst.,* **34**, 1894 (2012).

18) K. Ichimiya: *Concrete J.,* **55**, 131 (2017).

19) K. Ichimiya, S. Hatanaka and D. Atarashi: *Concrete J.,* **56**, 409 (2018).

20) I. Ellithy, M. Esguerra and R. Radhakrishnan: *AIP Advances,* **15**, 035205 (2025).

21) S. Tajima, S. Inoue and Y. Kano: *Proc. Jpn. Concr. Inst.,* **47**, 870 (2025).

22) H. Masumoto and T. Yamamoto: *J. Jpn. Inst. Met. Mater.,* **1**, 135 (1937).

23) Japan Society of Civil Engineers: "Report of the Research Subcommittee for Promoting the Practical Use of Geopolymer Technology in the Civil Engineering Field (361 Committee)" (2022),

24) Japan Concrete Institute: Committee Report "Report of the Research Committee on the Application of Geopolymer Technology to the Construction Industry" (2017),

25) M. Uehara, K. Minami, H. Hirata and A. Yamazaki: *Proc. Jpn. Concr. Inst.,* **37**, 1987 (2015).

26) K. Minami, T. Matsubayashi and M. Funahashi: *Proc. Jpn. Concr. Inst.,* **35**, 1957 (2013).

27) J. C. Maxwell: A treatise on Electricity and Magnetism, Oxford, Vol. 1, 3rd ed. (1904) 441.

28) K. Sun, Y. Li, S. Feng, Q. Gao, Z. Wang, X. Wei, L. Ju and R. Fan: *J. Electron. Mater.,* **50**, 1467 (2021).

29) R. M. Bozorth: Ferromagnetism, Wiley-IEEE Press, (1951)

30) T. Shimomura: *Concrete J.,* **43**, 56 (2005).

31) I. Ellithy, M. Esguerra and R. Radhakrishnan: *J. Appl. Phys.,* **135**, 205104 (2024).

32) R. E. Alley and V. E. Legg: *J. Appl. Phys.,* **31**, S239 (1960).

33) V. Tsakaloudi, D. Holz and V. Zaspalis: *J. Mater. Sci.,* **48**, 3825 (2013).

Received Jul. 10, 2025; Accepted Sep. 16, 2025

INDEX

J. Magn. Soc. Jpn., **50**, 19-22 (2026)

<Paper>

Micromagnetic simulation of influence of microstructure parameters on realization of high coercivity state in hard-magnetic MnAl alloys

E.A. Smirnov, M.V. Gorshenkov

National University of Science and Technology MISIS*, 119049, Moscow, Russia*

Micromagnetic simulation was employed to investigate the influence of microstructure parameters on the realization of high coercivity in nanocrystalline MnAl alloys, a promising alternative to rare-earth-based permanent magnets. The study focused on the effects of crystallite size (10–200 nm) and intergrain layer properties (non-ferromagnetic and soft-magnetic) on coercive force (Hc) and remanent magnetization (M_r/M_s). Simulations were performed using GPU-accelerated mumax3 software, with material parameters set to match MnAl (K_{u1} = 1.5 MJ/m^3, A_{ex} = 19.9 pJ/m, M_{sat} = 0.66 MA/m). Results revealed that the highest coercivity (μ_0H_c = 0.5 T) was achieved for crystallite sizes between 30–90 nm, consistent with experimental literature. The shape of the crystallites (cubic vs. cylindrical) showed negligible influence except for larger sizes (200 nm). For non-ferromagnetic interlayers, coercivity peaked at 0.52 T with a 7-nm thickness, attributed to the magnetic isolation of crystallites, while thicker layers with reduced H_c could be associated with changes in magnetic interaction between crystallites. In contrast, soft-magnetic interlayers (α-Fe) caused a monotonic decline in both H_c and M_r/M_s with increasing thickness. These findings provide critical insights for optimizing MnAl-based magnets, highlighting the importance of crystallite size control and interlayer engineering in achieving high coercivity.

Keywords: micromagnetic simulation, crystallite size, intergrain layers, hard-magnetic alloys, MnAl alloys.

1. Introduction

Recently, manganese-based permanent magnet materials have garnered significant attention due to their potential to bridge the performance gap between low-cost ferrites and high-performance rare-earth metal (REM)-based magnets, particularly in applications where energy densities around 100 kJ/m^3 are required[1),2)]. These materials, such as MnAl alloys, offer a compelling advantage: they are composed of abundant and inexpensive raw materials, making them a cost-effective alternative to REM-based magnets[3)]. This is especially relevant for applications like electric motors in transport systems, where miniaturization is not a critical requirement[4)].

The MnAl system exhibits high uniaxial magnetocrystalline anisotropy with typical constant ranging K_1 = 1.525 MJ/m^3, which can be tuned by proper alloying[5)], a property essential for achieving high coercivity in permanent magnets. However, realizing optimal magnetic performance in these alloys depends heavily on microstructure parameters, such as crystallite size[6)], crystalline defects[7)] and boundary conditions[8)]. Previous studies have highlighted the importance of nanocrystalline structures in enhancing coercivity[9)], but the specific role of intergrain layers—whether non-ferromagnetic or magnetically soft—remains less explored.

This study employs micromagnetic simulation to investigate the influence of crystallite size and interlayer thickness on the magnetic properties of MnAl alloys. By analyzing coercive force (H_c) and remanent magnetization (M_r/M_s), we aim to identify the optimal microstructure parameters for achieving a highly coercive state. The findings will contribute to the development of MnAl-based magnets with tailored properties, offering a viable alternative to REM-dependent technologies.

2. Experimental

Micromagnetic simulations were performed using the GPU-accelerated micromagnetic software mumax3[10)]. The MnAl material was modeled as a polycrystal, with crystallite shapes and sizes defined by Voronoi tessellation. We create a finite element mesh of the described model, with cell size of 3.5 nm, boundary conditions for computing the magnetostatic potential, can be treated at infinity[10)]. To account for material inhomogeneity, the magnetocrystalline anisotropy constant was varied by 10% across the structure. The direction of the easy axis was randomly set in each crystallite to bring the model closer to the polycrystalline sample. Therefore, it does not matter in which direction the external magnetic field is applied in. The initial magnetization of the crystallites was set randomly as in polycrystal, and the system was relaxed ($M_r/M_s \approx 0$) before computing the hysteresis loop. An external magnetic field was applied along the z-axis, ranging from 0 T to 6 T in steps of 0.2 T. After each field step, the system was energy-minimized, and the total magnetization was recorded. The material parameters used were consistent with MnAl alloys: K_{u1} = 1.5 MJ/m^3, A_{ex} = 19.9 pJ/m, M_{sat} = 0.66 MA/m[11)].

To validate the model, the coercive field dependence on crystallite size (ranging from 10 nm to 200 nm) was calculated for two geometries of equal volume: a cylinder (with 350 nm radius and 700 nm height) and a cube (cube-sided 630 nm), then compared with reference

---

Corresponding author: E.A. Smirnov (e-mail: m2005318@edu.misis.ru).

data3). In this case we also used scale exchange function to reduce exchange coupling from 1 to 0.9 between two regions to simulate crystallite boundaries.

Since mumax3 does not natively support interlayer modeling, an additional Python script was developed to systematically vary the interlayer thickness in steps matching the cell size (3.5 nm). The step of change in the thickness of the interlayer is determined by the Bloch parameter, in our case $\delta_0 = 3.64$ nm. For simulation it is necessary to use the cell size smaller than δ_0, for optimization of calculations according to the article10) the size of 3.5 nm was chosen. This allowed investigation of the interlayer's influence on hysteresis properties. It is important to note that in this case scale exchange function was no longer used, exchange coupling was set as default.

The Henkel plots were constructed based on the methodology described by Kelly12). To plot the dependence of the remanent magnetization from the demagnetized state $M_j(H)$, the sample is magnetized in a positive external field H_1; then the field is reduced to zero, and the obtained value of the remanent magnetization $M_j(H_1)$ is recorded. This procedure is repeated until the external magnetizing field H_1 reaches the selected maximum value H_{max} with a specified step. To determine the dependence of the remanent magnetization from the magnetized state $M_d(H)$ on the external magnetic field, the sample is first magnetized in a field with the maximum value H_{max}. A negative field $-H_1$ is then applied, after which the field is increased back to zero, and the resulting remanent magnetization value $M_d(H_1)$ is recorded. This procedure is repeated until the magnetizing field $-H_1$ reaches the maximum value $-H_{max}$.

The obtained magnetization values $M_j(H_1)$ and $M_d(H_1)$ are normalized to $M_{inf}(H)$, and then then plots the dependence of $M_d(H)/M_{inf}(H)$ and $M_j(H)/M_{inf}(H)$ versus applied magnetic field.

3. Results and discussion

As a first step of our work the model for simulation was verified by hysteresis loop calculations for different crystallite sizes for models without any interlayer. The result is the coercive force dependence on the crystallite size (Fig. 1(a)), that qualitatively and quantitatively coincide with the data published in article3) for the crystallite size ranging 10-200 nm. Also, hysteresis loops are shown for a crystallite size of 50 nm for cubic and cylindrical shapes as an example of the data obtained as a result of the calculations (Fig. 1(b)). As can be seen, changing the shape of the model from cylinder to cube significantly affects the coercive force only at a crystallite size larger than 200 nm. The coercive force μ_0H_c decreases from 0.452 T to 0.302 T. Similarly, a small difference in the magnitude of the coercive force (0.516 T for the cubic versus 0.497 T for the cylinder) is observed at a crystallite size of 30 nm. The effect is not quite explained yet, it will be investigated in more detail in future work. Most likely, the difference for 200 nm crystallite size arises due to the limited number of crystallites (about 30 pcs.), which are placed in the model. As a consequence, the condition of chaotic disorientation of crystallites is not fulfilled, which leads to significant changes in the coercive force.

For further study of the influence of the interlayer on the magnetic properties, a cubic shape model was chosen because of the feature of the self-written script for creating a layer of different thickness between the crystallites. The calculations of interlayer thickness influence were conducted at a crystallite size of 90 nm, since this is the largest size at which the maximum coercivity is preserved. Magnetic hysteresis loops were calculated for ensembles with different thicknesses of the intergrain (in this study, the terms 'grain' and 'crystallite' are used synonymously, the term 'intergrain' is employed throughout for its precision and widespread acceptance in the literature) interlayer: 3.5 nm, 7.0 nm, 10.5 nm, 14.0 nm, as well as without interlayer (Fig. 2).

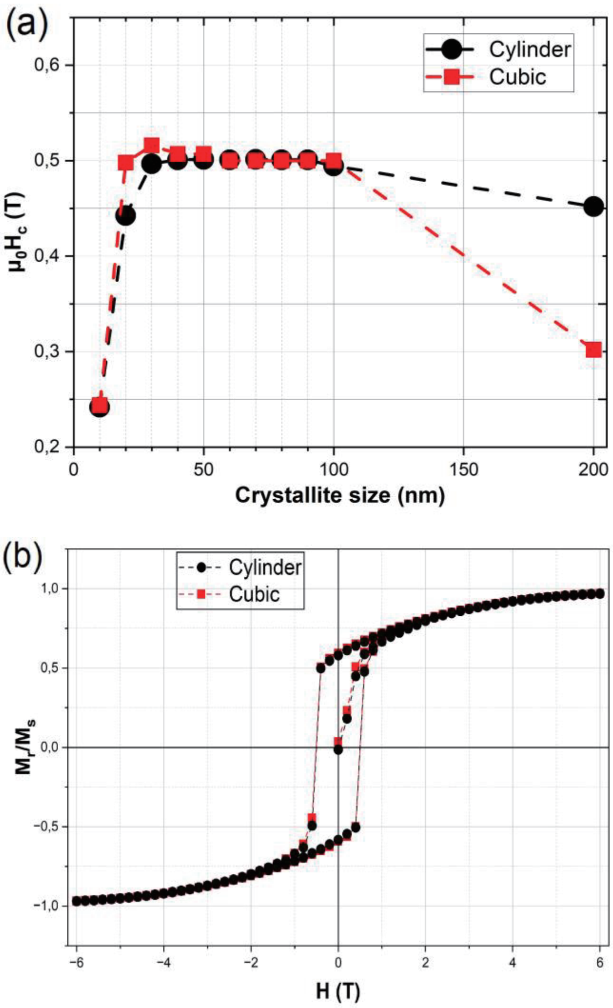

Fig. 1 (a) Coercive force μ_0H_c dependence on crystallite size for models without any interlayer. (b) hysteresis loop for crystallite size 50 nm without any interlayer.

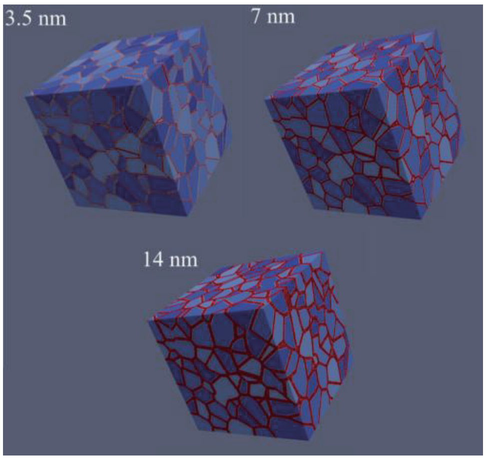

Fig. 2 Examples of intergrain interlayer (red color) with different thicknesses.

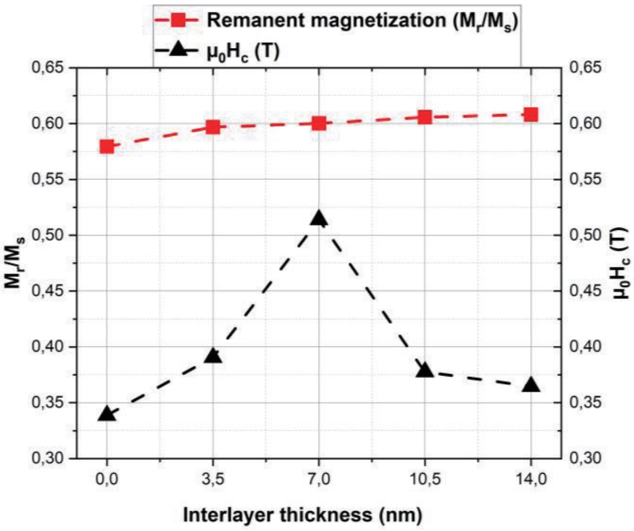

Fig. 3 Plots of coercivity and remanent magnetization dependence on thickness of non-ferromagnetic interlayer.

Non-ferromagnetic and magnetically soft interlayers were investigated. As the material for the magnetically soft interlayer α-Fe (K_{c1} = 48 kJ/m3, M_{sat} = 1.7 MA/m) was chosen, for the simulation of a non-ferromagnetic interlayer, the magnetic parameters were not declared, which corresponds to the existence of non-ferromagnetic phase between ferromagnetic crystallites.

Figure 3 shows that the coercive force first increases with the thickness of the non-ferromagnetic interlayer. The maximum μ_0H_c=0.52 T is observed at a thickness of 7 nm. The mechanism is not quite clear, presumably there is an effect of magnetic isolation of crystallites. Further decrease in the coercive force could be associated with a change of magnetic interaction between the crystallites. Henkel plots were constructed for layer thicknesses of 3.5 and 14 nm to test this assumption (see fig. 5(a)). The remanent magnetization increases steadily with increasing thickness of the interlayer because the crystallites become more and more isolated and the processes of remagnetization in each of them practically do not affect the others.

In Figure 4, the coercive force decreases as the thickness of the magnetically soft interlayer increases, but there is no increase in the remanent magnetization. When the thickness of the interlayer is increased up to 7 nm, the value of the remanent magnetization is practically unchanged and then begins to decrease. Consequently, no increase in the residual magnetization due to the influence of the magnetically soft phase was achieved.

Henkel plots were constructed using the methodology described in the experiment chapter for the models with non-ferromagnetic interlayer thicknesses of 3.5 and 14 nm. To optimize the computational algorithm and reduce the requisite number of calculations, pre-saved magnetization state files were used. These files represented the system in both the demagnetized state and the state of magnetic remanence following saturation. The results are shown in Figure 5 (a).

Analysis of the field dependence shows that the $M_j(H)/M_{inf}(H)$, demonstrates continuous positive growth for both noon-ferromagnetic layer thicknesses (14 nm and 3.5 nm). In contrast, the $M_d(H)/M_{inf}(H)$, displays a monotonic decrease, transitioning to negative values at applied fields greater than 0.4 T. To analyze the intergrain interaction, the Kelly $\delta_m(H)=M_d(H)/M_{inf}(H)-(1-2 \cdot M_j(H)/M_{inf}(H)))$ plots on the field value were constructed, see Fig. 5 (b). As can be seen from the figure, the values of $\delta_M(H)$ in the whole region take positive values, which indicates that exchange coupling between ferromagnetic crystallites is dominant over the dipolar interaction[13]. The peak intensity was markedly higher for the 3.5 nm interlayer

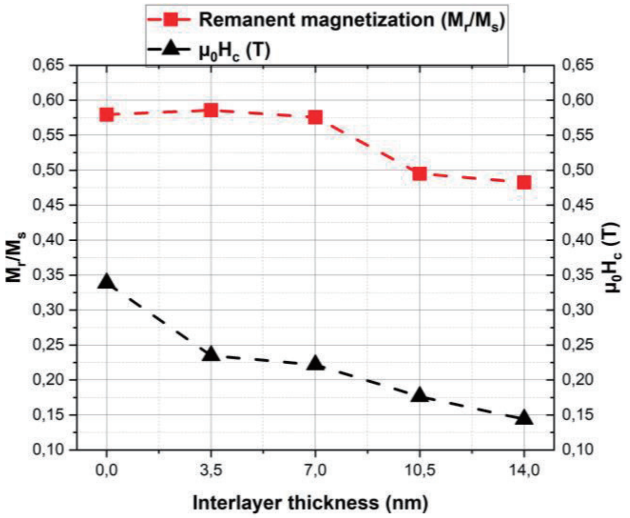

Fig. 4 Plots of coercivity and remanent magnetization dependence on thickness of soft-magnetic interlayer.

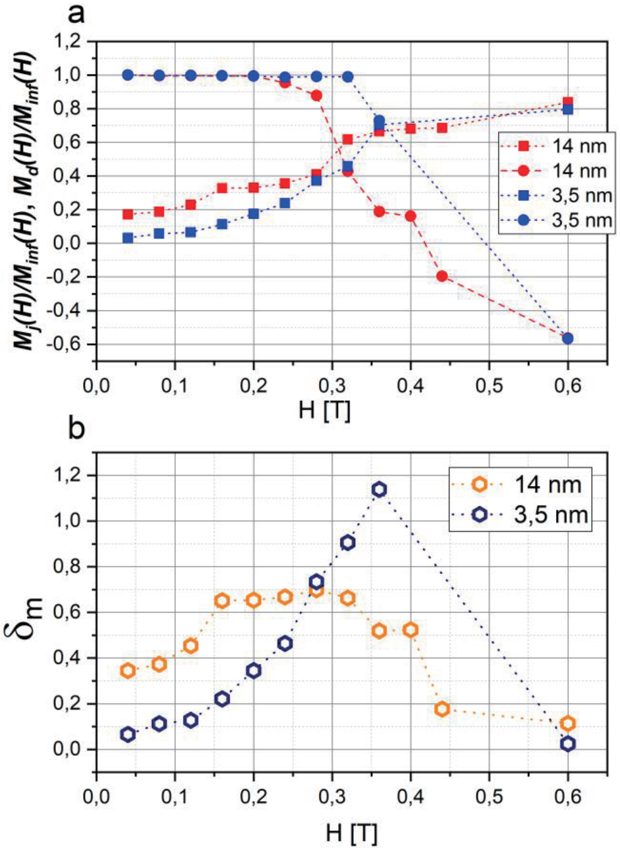

Fig. 5 Henkel plots (a) and Kelly $\delta_m(H)$ plots (b). for models with non-ferromagnetic interlayer thicknesses of 3.5 and 14 nm.

relative to its 14 nm counterpart.

The following assumptions can be put forward as possible reasons for such behavior of the coercive force. The extremal dependence of coercivity on interlayer thickness is explained by considering two competing physical pathways. Primarily, with an increase in the interlayer thickness, the average crystallite size decreases due to the fact that the interlayer is specified by redesignation of the cells at the boundary of the crystallites during computational analysis. For example, for a 14 nm thick interlayer, this value is subtracted from the average crystallite size. Thus, for a larger interlayer, the real crystallite size becomes smaller by the interlayer value. Interlayer thickness increasing leads to a decrease in exchange coupling between ferromagnetic crystallites. Conversely, enhanced isolation of crystallites tends to increase the coercive force, whereas the concurrent reduction in intercrystallite magnetic interactions tends to decrease it. However, the put forward assumption requires detailed verification and additional calculations.

4. Conclusion

In this work, the aim was to establish the optimal structure parameters for the realization of a highly coercive state in an alloy with a nanocrystalline structure, as well as to investigate the influence of the intergrain interlayer on magnetic properties. The following conclusions can be drawn based on the work results:

1. For ensembles of ferromagnetic particles with high magnetocrystalline anisotropy of cubic and cylindrical shape, a graph of the dependence of the coercive force H_c on the crystallite size d is plotted. The highest value of coercive force ($\mu_0 H_c$=0.5 T) is achieved at crystallite size from 30 nm to 90 nm (Fig. 1). The results obtained correlate with the literature data plotted based on experimentally obtained values3).
2. The crystallite size range from 90 nm to 30 nm should be used to give a highly coercive state to the ferromagnetic alloy of the Mn-Al.
3. On the obtained magnetic hysteresis loops for ensembles with a layer imitating a non-ferromagnetic insulating boundary, the coercivity has a maximum ($\mu_0 H_c$=0.52 T) at a layer thickness of 7 nm, presumably there is an effect of magnetic isolation of crystallites. Further decrease in the coercive force could be associated with a change of magnetic interaction between the crystallites. (Fig. 3).
4. The obtained magnetic hysteresis loops for models with different thicknesses of the magnetically soft interlayer show a sharp drop in the coercivity value with increasing interlayer thickness; the residual magnetization also decreases (Fig. 4).

Further, it is planned to develop a model that considers the influence of crystallite structure defects, especially the influence of twins, to explain the low values of coercivity.

Acknowledgements The study was supported by the Russian Science Foundation, project no. 23–13–00161 https://rscf.ru/project/23–13-00161/.

Special thanks to AMT&C group of companies for help with participation at IcAUMS2025 with this work.

References

1) J.M.D. Coey: *Scr. Mater.*, **67**, 524 (2012).
2) T. Keller, I. Baker: *Prog. Mater. Sci.*, **124**, 100872 (2022).
3) Y. Jia et al.: *Acta Mater.*, **245**, 118654 (2023).
4) S. Kontos et al.: *Energies*, **13**, 5549 (2020).
5) M. Choi et al.: *J. Magn. Magn. Mater.*, **589**, 171513 (2024).
6) Y. Jia: *Intermetallics*, **96**, 41 (2018).
7) F. Bittner: *J. Alloy. Comp.*, **704**, 528 (2017).
8) S. Bance: *Acta Mater.*, **131**, 48 (2017).
9) A. Chaturvedi: *Metals*, **4**, 20 (2014).
10) A. Vansteenkiste et al.: *AIP Adv.*, **4**, 107133 (2014).
11) J. Thielsch, F. Bittner, T.G. Woodcock: *J. Magn. Magn. Mater.*, **426**, 25 (2017).
12) P.E. Kelly et al.: *IEEE Trans. Magn.*, **25**, 3881 (1989).
13) H. Zhang et al.: *Appl. Phys. Lett.*, **82**, 4098 (2003).

Received May 29, 2025; Revised Jul. 17, 2025; Accepted Oct. 31, 2025

INDEX

J. Magn. Soc. Jpn., **50**, 23-29 (2026) <Paper>

Improving magneto-optical properties of $Nd_{0.5}Bi_{2.5}Fe_5O_{12}$ thin films by introducing $Bi_3Fe_5O_{12}$ underlayer

J. Zhang, K. Watanabe, F. Z. Chafi, M. Nishikawa, H. Asada*, M. Kawahara**, M. Veis***, and T. Ishibashi

Department of Materials and Bioengineering, Nagaoka Univ. of Tech., *1603-1 Kamitomioka, Nagaoka, 940-2188, Japan*
*Graduate School of Science and Technology for Innovation, Yamaguchi Univ., *2-16-1 Tokiwadai, Ube, Yamaguchi 755-8611, Japan*
**Kojundo Chemical Laboratory Co., Ltd., *Chiyoda, Sakado, Saitama 350-0214, Japan*
***Faculty of Mathematics and Physics, Charles Univ. of Prague, *Prague 2, Czech Republic*

To improve the magneto-optical properties of $Nd_{0.5}Bi_{2.5}Fe_5O_{12}$ (Bi2.5:NIG) thin films, a $Bi_3Fe_5O_{12}$ (BIG) underlayer was introduced. Bi2.5:NIG thin films with a thickness of 150 nm were prepared on $Nd_2BiFe_4GaO_{12}$(Bi1Ga1:NIG)/BIG layers prepared on glass substrates, and Bi2.5:NIG/BIG layers were prepared on $Gd_3Ga_5O_{12}$(GGG)(100) substrates, where all samples were prepared by using the metal-organic decomposition method. The Faraday rotation angle at around a wavelength of 520 nm significantly increased from 16.7°/μm to 31.5°/μm for Bi2.5:NIG/Bi1Ga1:NIG/BIG/glass and from 18.5°/μm to 27.8°/μm on Bi2.5:NIG/BIG/GGG. We consider the improvement in the Faraday rotation angles of these samples' BIG underlayer to have enhanced the epitaxial growth of Bi2.5:NIG, resulting in an improved crystallinity and Faraday effect for the Bi2.5:NIG thin films.

Keywords: Bi-substituted Nd iron garnet, metal organic decomposition, underlayer introduction, surface diffusion, crystallinity, Faraday effect

1. Introduction

Bismuth-substituted rare-earth iron garnet, $R_{3-x}Bi_xFe_5O_{12}$ (Bix:RIG), has properties such as high transmittance and large magneto-optical (MO) effect in the visible light region, where Bi^{3+} substitutes the rare earth ion R^{3+}. The MO effect is dramatically improved with increasing Bi content[1-5] because of the spin-orbit interaction between the 6p orbital in Bi^{3+} and the 2p orbital in O^{2-}. The excellent MO effect has led to its application in various magneto-optical devices such as optical isolators, MO spatial light modulators for application in 3-D holographic displays and MO imaging technology [6-11].

Our group has previously developed the fabrication technique of iron garnet thin films using the metal-organic decomposition (MOD) method[12] and succeeded in preparing high-quality $Y_{3-x}Bi_xFe_{5-y}Ga_yO_{12}$ and $Nd_{3-x}Bi_xFe_{5-y}Ga_yO_{12}$ thin films on $Gd_3Ga_5O_{12}$ (GGG) single-crystal substrates[13,14]. Furthermore, we have succeeded to obtain garnet films on glass substrates with Bi content of $x \geq 2$, which are metastable materials[15-17]. In the fabrication of Bi2.5:NIG thin films, $Nd_2BiFe_4GaO_{12}$ (Bi1Ga1:NIG), which is a stable material, is used for buffer layers on glass substrates.

In this study, we have chosen $Nd_{0.5}Bi_{2.5}Fe_5O_{12}$ (Bi2.5:NIG), despite its lower Faraday rotation angle compared to $Bi_3Fe_5O_{12}$ (BIG), as Bi2.5:NIG has an excellent magneto-optical figure of merit (FOM) and exhibits a larger FOM than BIG[17]. In magneto-optics, figure of merit (FOM)[18,19] is used to evaluate the performance of magneto-optical materials by quantifying their Faraday rotation and optical absorption at a given wavelength, and it can be expressed as follows:

$$FOM = \frac{\theta_F}{\alpha}, \qquad (1)$$

where θ_F is Faraday rotation (in radians or degrees), and α is the optical absorption coefficient (in cm^{-1}).

In addition, BIG suffers from lower crystallinity, a higher absorption coefficient in the visible range, and difficulties in controlling magnetic anisotropy[20,21]. It has been reported that Bi2.5:NIG exhibits Faraday rotation angle of 20°/μm at a wavelength of 520 nm. However, we consider that there is a possibility to improve the MO properties of Bix:RIG by improving crystallinity. Because Bi^{3+} substitution decreases the crystallinity of Bix:RIG films[22], further processing improvements are necessary.

In the MOD method, garnet crystal is obtained by annealing precursor prepared by decomposing metal-carboxylates at annealing temperature of ~450 ℃. In a process of the crystallization at annealing temperature of 600 – 700 ℃, for example of Bi2.5:NIG films on GGG substrates, Bi2.5:NIG crystals start to grow from the surface of GGG substrates, and the crystal grows up to the film surface. To improve its crystallinity even in the solid-state reaction, enhancing diffusion length of constituent metal ions at the surfaces of growing crystals in precursor is significant. In general, an annealing temperature for crystallization should be increased to increase the surface diffusion length of the constituent metal ions. However, a higher annealing temperature may cause secondary phases such as Fe oxides.

Several techniques that enhance crystal growth

Corresponding author: T. Ishibashi
(e-mail: t_bashi@mst.nagaokaut.ac.jp).

utilizing characteristics of Bi, such as a liquid phase epitaxy, a surfactant epitaxy, were reported [23,24]. In this study, we propose a method that uses BIG underlayers for Bi2.5:NIG thin films. We consider that enhancing diffusion of constituent metal ions during the crystal growth can be achieved without increasing annealing temperature by increasing Bi content. This is because we believe that the reason the crystallization temperature decreases when the Bi composition is increased[25] is because the diffusion length of ions during crystallization increases. If this idea is correct, it should improve the crystallinity of the garnet crystals grown on the GGG substrate in the early stages and thus the crystallinity of the entire thin film. In addition, since BIG has the same lattice constant as that of Bi2.5:NIG, which is also important factor to increase crystallinity of Bi2.5:NIG thin films.

In this paper, we report on the improvement of crystallinity and MO effects of Bi2.5:NIG thin films with BIG underlayer grown on glass and GGG substrates.

2. Experiment

In this study, we used MOD solutions containing metal carboxylates with 4% dissolved in organic solvents. Specifically, we used the MOD solutions with compositions of Nd : Bi : Fe : Ga = 2 : 1 : 4 : 1, Nd : Bi : Fe = 0.5 : 2.5 : 5, Nd : Fe = 3 : 5, Nd : Fe = 3 : 5 and Bi : Fe = 3 : 5, produced by Kojundo Chemical Laboratory Co., Ltd., Sakado, Japan, to prepare Bi1Ga1:NIG, Bi2.5:NIG, $Nd_3Fe_5O_{12}$ (NIG) and BIG, respectively. The glass substrates used were "EAGLE XG glass substrates with (10 mm × 10 mm × 0.7 mm) (from Corning Inc., Corning, NY, USA)". The "GGG (100) single-crystal substrates (10 mm × 10 mm × 0.5 mm) (from SAINT-GOBAIN, Courbevoie, France)".

In the fabrication process, MOD solutions were spin-coated onto substrates at 3000 rpm for 30 seconds. The coated films were then dried at 100 °C for 10 min, followed by pre-annealing and final annealing processes.

For the buffer layer (Bi1Ga1:NIG), the coating and pre-annealing process was repeated three times, with each cycle involving pre-annealing at 430 °C for 10 min. After the final coating cycle, a final annealing was performed at 650 °C for 3 hours in ambient air.

For the subsequent garnet films (e.g., Bi2.5:NIG, NIG, and BIG), whether deposited on top of the buffer layer or directly on the substrate, pre-annealing was conducted at 450 °C for 10 min, followed by final annealing at 640 °C for 3 hours in ambient air as well.

To avoid confusion, hereafter we will refer to the Bi1Ga1:NIG layer as a "buffer layer".

We defined "1 layer" as a film obtained by a single coating of MOD solution, whose thickness is 20 nm – 40 nm, depending on the composition. We also defined "2 layers", "5 layers" and "6 layers" as films obtained by two, five and six repetitions of the spin coating of MOD solutions and pre-annealing, respectively. An annealing for crystallization was subsequently carried out. The annealing of the BIG underlayer was carried out simultaneously with the overlying film.

Various structures were prepared, with samples A-F on glass substrates and samples G – H on GGG substrates (Fig.1). Buffer layers were used for samples A-F, with BIG single layer for samples B, C, F, and BIG double layer for sample D. NIG single layer was added in samples C and D. Bi2.5:NIG was deposited in multiple layers for samples E and F, while Bi2.5:NIG and Bi2.5:NIG/BIG films were prepared on GGG substrates for samples G and H. Sample A was a buffer layer, which was used for a reference of the garnet structure, and sample B was prepared to show that BIG with the garnet structure cannot be obtained with the annealing process described above. Sample C was prepared to examine the role of BIG underlayer, sample D tested its thickness effect on film formation. Samples E-H assessed the BIG underlayer's impact on crystallinity and magneto-optical properties.

The samples were evaluated using the following characterization techniques: X-ray diffraction (XRD) to identify crystal phases, a MO spectrometer to measure Faraday rotation angle, cross-sectional transmission

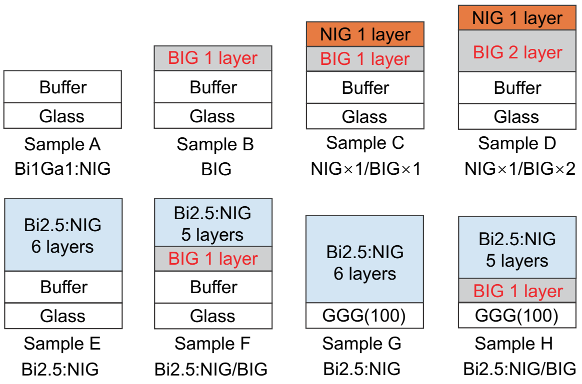

Fig. 1 Schematic illustration of samples prepared by MOD method.

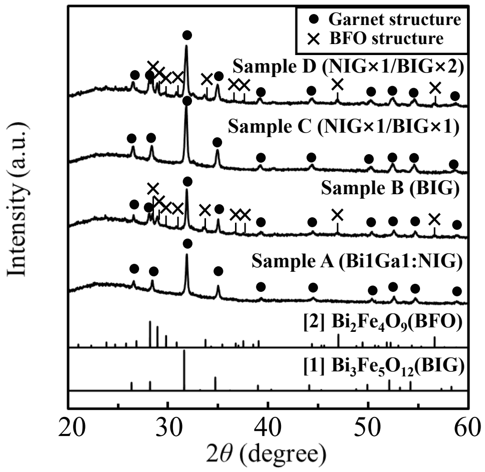

Fig. 2 XRD patterns obtained using Cu-Kα radiation (λ = 0.154 nm) for sample A (Bi1Ga1:NIG), sample B (BIG), sample C (NIG×1/BIG×1), and sample D (NIG×1/BIG×2).

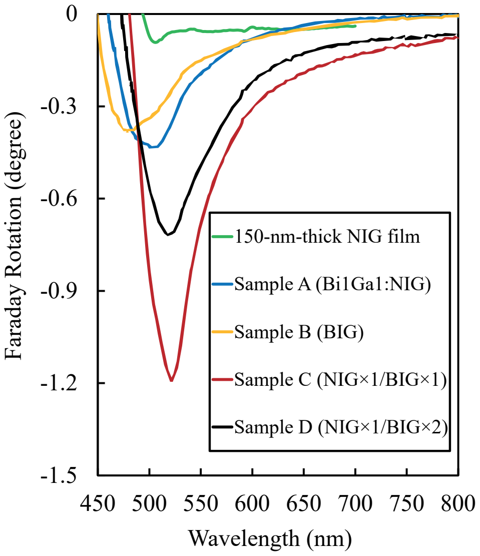

Fig. 3 Faraday spectra measured under a magnetic field of 2.6 kOe for sample A (Bi1Ga1:NIG), sample B (BIG), sample C (NIG×1/BIG×1), sample D (NIG×1/BIG×2), and 150-nm-thick NIG film.

electron microscopy (TEM) and energy-dispersive spectroscopy (EDS) to analyze microstructure and composition, ferromagnetic resonance (FMR) to assess magnetic uniformity, and atomic force microscopy (AFM) to observe surface morphology. These measurements were essential to comprehensively understand the structural, magnetic, and MO properties of our samples.

3. Results and discussion

3.1 NIG/BIG thin films on glass substrates

Figure 2 displays the XRD patterns for samples A–D, obtained using Cu-Kα radiation (λ = 0.154 nm), along with reference data for BIG and $Bi_2Fe_4O_9$ (BFO) 26-27). It can be observed that buffer layer (sample A) has a polycrystalline garnet structure. In addition to a garnet structure (closed circle marks), a secondary phase was found in sample B (cross marks) that was estimated to be BFO. Since buffer layer was expected to exhibit a garnet structure, the BFO structure is formed from the BIG layer. For sample C, an NIG layer with BIG underlayer, the XRD pattern indicated diffraction pattern of garnet structure, and no secondary structure was observed. However, in sample D, an NIG layer with double BIG underlayers, diffraction pattern of BFO was observed in addition to the garnet structure.

Figure 3 shows the Faraday rotation spectra measured under a magnetic field of 2.6 kOe of samples A – D, and a 150 nm-thick NIG film was prepared the same way in our laboratory and used as a reference. This is just to show that the contribution of NIG to the overall Faraday rotation angle is negligible and thus does not significantly affect the experimental results. All spectra of samples A-D exhibited characteristics of the Bi-substituted iron garnet. Sample A has a peak of Faraday rotation angle of $\theta_F = -0.44°$ at 503 nm, which is consistent with that of buffer layer. Samples C and D exhibited $\theta_F = -1.19°$ and $\theta_F = -0.72°$ at 521 nm, respectively. In the visible light region, Bi-substituted garnet films usually exhibit a Faraday rotation peak around 500 - 530 nm, and the rotation angle gradually decreasing as the wavelength increases. With increasing Bi content, the peak shifts to longer wavelengths, and BIG shows a peak around 530 nm, with a Faraday rotation angle of 30°/μm. However, in sample B, both the peak wavelength and the Faraday rotation angle are almost the same as those of sample A, which does not indicate the formation of BIG. This result suggests that the BIG under layer was not crystallized properly under annealing conditions of 640 °C, which is consistent with XRD results showing existence of a secondary phase, and with the fact that BIG can be typically crystallizes at a temperature as low as 490 °C 28). On the other hand, Faraday rotation angle of sample C, consisting of a single BIG underlayer and a single NIG layer above buffer layers, was larger than that of sample B. In addition, a peak position of the Faraday spectrum for sample C is located around 520 nm, which is close to the peak of the Bi2.5:NIG. This means that apart from the small Faraday rotation angle of the NIG added to sample B, there is another reason for the large rotation angle. We consider that the observed increase in the θ_F can be attributed to the formation of a Bi-substituted garnet structure from the NIG layer and BIG underlayer. Considering that sample C has the garnet structure without secondary phases as observed in XRD measurement shown in Fig.2, the Bi-substituted garnet should grow epitaxially on the buffer layer. Therefore, it is considered that Nd^{3+} in the NIG layer diffused to the interface between the BIG underlayer and the buffer layer. This diffusion raised the crystallization temperature at the interface, enabling crystallization to occur at 640 °C and achieved crystal growth.

However, in the case of sample D which has double

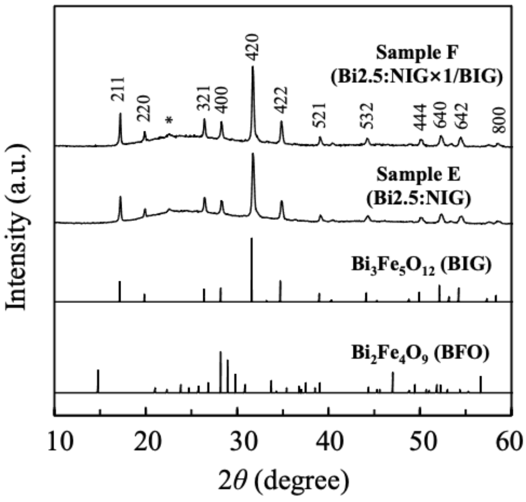

Fig. 4 XRD patterns obtained using Cu-Kα radiation (λ = 0.154 nm) for sample E (Bi2.5:NIG) and sample F (Bi2.5:NIG/BIG).

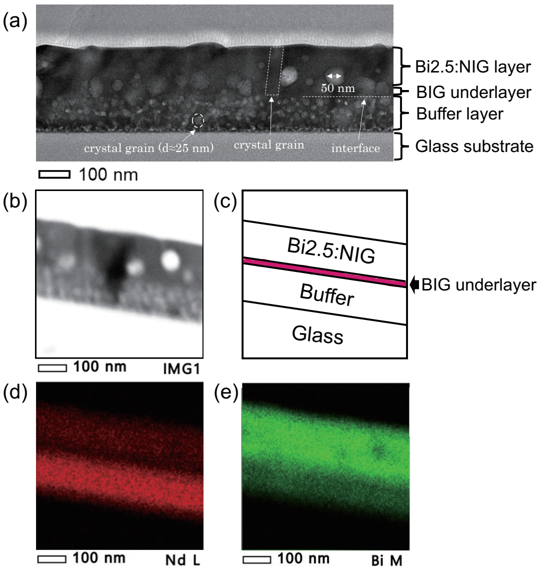

Fig. 5 (a) shows TEM cross-sectional image of sample F (Bi2.5:NIG/BIG), (b) presents TEM cross-sectional image used for TEM-EDS elemental mapping, (c) provides schematic illustration of material composition at different cross-sectional positions indicated in (b), while (d) and (e) respectively display elemental mappings of Nd and Bi.

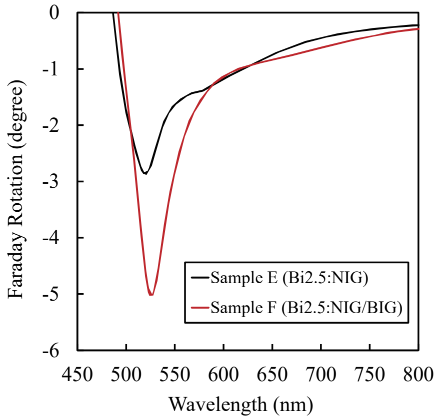

Fig. 6 Faraday spectra measured under a magnetic field of 2.6 kOe for sample E (Bi2.5:NIG) and sample F (Bi2.5:NIG/BIG).

BIG underlayers, the Faraday rotation angle became smaller than that of sample C, although the amount of Bi was larger. However, the Faraday rotation angle of sample D remains larger than that of the buffer layers, indicating that a Bi-substituted iron garnet structure is formed above the buffer layers. The decrease of Faraday rotation angle can be understood from the fact that a secondary phase, BFO, was observed by XRD. If the considerations regarding sample B are correct, it is believed that the thicker BIG layer in sample D prevented Nd ions from sufficiently diffusing to the surface of the buffer layer. As a consequence, BFO was found in XRD measurement.

Based on this result, a single layer of BIG underlayer is used for Bi2.5:NIG thin film in the next experiment.

3.2 Bi2.5:NIG/BIG thin films on glass substrates

Figure 4 shows the XRD patterns obtained using Cu-Kα radiation (λ = 0.154 nm) of samples E, F, and literature values of BIG and BFO. It was found that all peaks can be identified as a garnet structure except for a small peak at $2\theta = 23°$ that may be due to the secondary phase BFO. We considered that the secondary phase was formed due to excessive MOD solution at the edge of the samples when the MOD solution was spin coated.

Comparing intensities of 420 diffraction peaks, sample F has a higher intensity and a narrower full width at half maximum (FWHM) than sample E. The FWHM of 420 peaks are 0.27° and 0.24° for samples E and F, respectively. This result suggested the crystallinity of sample F was higher than that of sample E.

Figure 5 shows TEM cross-sectional images and elemental mappings of sample F. In the buffer layer, numerous crystal grains with an approximate diameter of 25 nm were observed. In the Bi2.5:NIG/BIG layer, columnar crystal grains extended from the buffer layer surface to the sample surface, and bright areas around 50 nm in size were also observed. The improved crystallinity of Bi2.5:NIG/BIG in sample F compared to Bi2.5:NIG in sample E suggests a potential interaction at the interface. In TEM images (Fig. 5), the boundary between BIG underlayer and Bi2.5:NIG layers appears indistinct, which could indicate such interdiffusion. This observation aligns with our earlier statements regarding the role of Bi in enhancing crystal growth and promoting interlayer interaction, thereby improving crystallinity through interdiffusion. Another important point is that without interdiffusion, the BIG underlayer cannot have a garnet structure, and as a result, the Bi2.5:NIG layer cannot have a garnet structure either. Figures 5(b) and (c) show TEM cross-sectional image of sample F measured for elemental mappings and a schematic illustration of the sample structure. Figures 5(d) and 5(e) shows elemental mappings of Nd and Bi measured for the area shown in Fig.5(b). Comparing the intensities of Nd

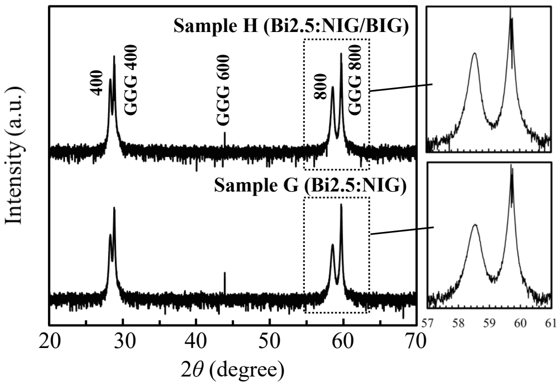

Fig. 7 $2\theta/\omega$ scan measured using Cu-Kα radiation (λ = 0.154 nm) for sample G (Bi2.5:NIG) and sample H (Bi2.5:NIG/BIG) on GGG (100) substrates.

and Bi at different cross-sectional positions, it's evident that for Nd concentration, the order is as follows: buffer layer > Bi2.5:NIG layer> BIG underlayer. In contrast, for Bi concentration, the order is: BIG underlayer > Bi2.5:NIG layer > buffer layer. Hence, BIG underlayer maintains a high concentration of Bi.

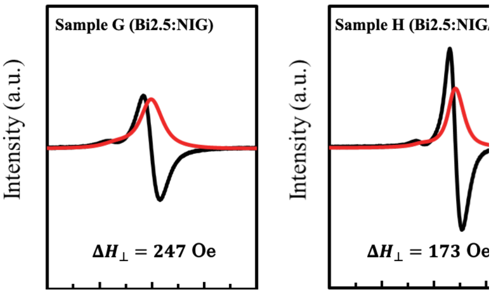

Fig. 8 FMR spectra of samples G (Bi2.5:NIG) and H (Bi2.5:NIG/BIG), measured under in-plane magnetic field applied to the samples at 9.09 GHz.

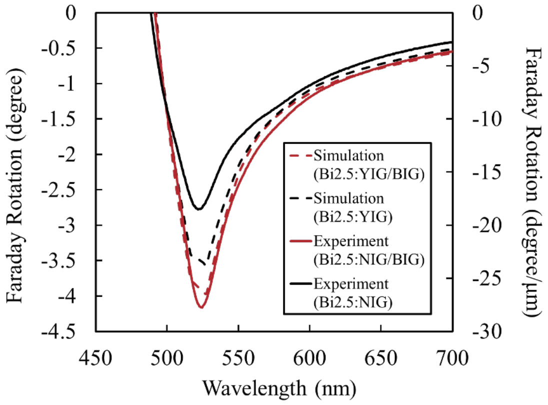

Fig. 9 Faraday spectra measured under a magnetic field of 2.6 kOe for sample G (Bi2.5:NIG) and sample H (Bi2.5:NIG/BIG).

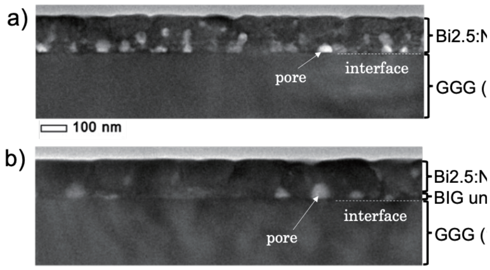

Fig. 10 Cross-sectional TEM images for (a) sample G (Bi2.5:NIG) and (b) sample H (Bi2.5:NIG/BIG).

Figure 6 shows Faraday spectra measured under a magnetic field of 2.6 kOe for samples E and F. The peak for sample F appears at a longer wavelength compared to sample E, likely due to its higher Bi content. At the same thickness, sample F exhibits a maximum Faraday rotation angle of $\theta_F = -5°$ at wavelength around 520 nm, compared to $\theta_F = -2.9°$ for sample E, an increase of approximately 72 %. The θ_F per unit thickness was improved from 16.7 °/μm to 31.5 °/μm by introducing BIG underlayer. In the spectral structure, sample E shows an interference peak at around 570 nm, which is not observed in sample F. Given the similar film thicknesses, this difference is likely due to variation in refractive index. As will be discussed later for samples E and F fabricated on single crystals, the BIG underlayer reduces void formation in the film, and because BIG and Bi2.5:NIG have higher refractive indices than air, the presence of voids would affect the overall index, causing this interference effect. However, determining precise optical constants by ellipsometry for films on glass substrates is challenging, so further study is required.

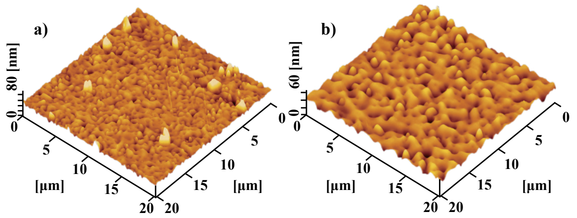

Fig. 11 Surface structure for (a) sample G (Bi2.5:NIG) and (b) sample H (Bi2.5:NIG/BIG) observed by AFM.

Notably, the difference in Faraday rotation angle between samples E and F at 520 nm is around 2°, which far exceeds the expected increase of 0.3° due to the insertion of BIG underlayer. This suggests that the significant increase in θ_F is mainly due to a combination of interference effects and improved crystallinity.

To further confirm the role of the BIG underlayer in improving the MO effect and crystallinity, the same experiment was conducted on GGG (100) substrates, and a simulation of the MO effects was performed.

3.3 Bi2.5:NIG/BIG thin films on GGG substrates

Figure 7 shows the XRD patterns obtained using Cu-Kα radiation (λ = 0.154 nm) for samples G and H prepared on GGG (100) substrates. Diffraction peaks indexed as 400 and 800 of the thin films were observed on the low angle side of those of the GGG (100) substrate, indicating that thin films with a garnet structure were grown along. FWHMs of 800 peaks of sample G and sample H were measured to be 0.27° and 0.2°, respectively, indicating that the peaks of sample H are sharper than those of sample G. As in the case of sample F prepared on glass substrate, the crystallinity of the film on the single substrate was improved by introducing BIG underlayer.

To evaluate the quality of the garnet thin films, FMR measurement[29-31] was also carried out. Figure 8 shows the FMR spectra of samples G and H, measured under an in plane magnetic field applied to the samples at 9.09 GHz, where the EPR signals originated to the GGG substrates have been subtracted. The black line shows measured signal, which is differential form of the FMR signal. The red line shows integral of measured FMR signals, indicating a microwave absorption. By comparing the resonance linewidths (ΔH) of samples G and H, with sample G at 247 Oe and sample H at 173 Oe, it is evident that sample H exhibits better magnetic uniformity which indicate sample H has better crystallinity. The narrower XRD peaks (Fig. 7), and the FMR linewidth (Fig. 8) confirm the improvement in crystallinity when introducing BIG underlayer. This suggests better structural and magnetic ordering and enhanced MO properties. Similar results were observed for glass substrates, where the BIG underlayer also contributes to improved crystallinity and magnetization properties. The consistency of these results across diffferent substrates (GGG and glass) underscores the fundamental role of the BIG underlayer in promoting crystallinity, demonstrating its effectivenes regardless of the substrate material, while reinforcing its significance in improving the overall film quality and performance.

Figure 9 shows the Faraday spectra measured under a magnetic field of 2.6 kOe of samples G and H. The peak of the Faraday spectra at around 520 nm of samples G and H were measured to be 2.8° and 4.2°, respectively. It is clearly seen that sample H has larger Faraday rotation per unit thickness around 27.8°/μm, which is larger than 18.5°/μm for sample G. For samples prepared on single crystal GGG substrates, the introduction of the BIG underlayer increased the Faraday rotation angle by more than 50%.

To investigate whether the improvement in MO effects is solely due to the increase in Bi concentration, we simulated the Faraday spectra for the Bi2.5:YIG/BIG film and the Bi2.5:YIG film with the same film structures of the samples G and H. Faraday rotation spectra were calculated by the matrix method[32)] using the dielectric tensors of BIG and Bi2.5:YIG[2)]. For the calculations, we used the dielectric constant tensor of Bi2.5:YIG, which has the same Bi composition as Bi2.5:NIG, but we believe this true as the MO effect is fundamentally determined by the Bi composition. Simulations can be considered as an ideal case, and it showed that the Faraday rotation angles at the peaks were 23.7°/μm and 26.7°/μm for Bi2.5:YIG and Bi2.5:YIG/BIG thin films, respectively. This difference is 12.7%, which is smaller than that of 50.3% between Bi2.5:NIG and Bi2.5:NIG/BIG thin films obtained experimentally. From this result, it is considered that the Faraday rotation angle of sample G is smaller than the ideal value. On the other hand, the value of sample H agrees well with the simulation result. From this, it is considered that the insertion of the BIG underlayer improved the crystallinity of the Bi2.5:NIG/BIG thin film, resulting in an ideal magneto-optical effect.

Figure 10 shows TEM cross-sectional images of samples G and H grown on GGG (100) substrates. It is evident that the cross-sectional images of the Bi2.5:NIG thin film prepared directly on the GGG substrate (sample G) displayed numerous white regions, particularly at the interface with the substrate. This observation indicates that a significant number of pores were formed during decomposition of metal carboxylates and the growth of the Bi2.5:NIG film along the GGG substrate surface, which can hinder uniform film growth. These issues are mitigated when the BIG underlayer is introduced promoting better crystal growth and more densification. Meanwhile, after the introduction of a BIG underlayer (Sample H), the white regions at the interface with the substrate were significantly reduced. Compared to Sample G, Sample H exhibited a more uniform crystalline structure and demonstrated improved crystallinity.

The surface structure of samples G and H observed in a 20 μm × 20 μm area by AFM are shown in Fig.11. The roughness of the sample G and sample H is 3.143 nm and 3.708 nm, respectively. The diameter of crystal grains on the surface for sample G and sample H is 0.5 μm and 1 μm, respectively. Sample H forms larger grains on the surface compared to sample G. Which confirms that the introduction of BIG underlayer promotes crystal growth and increases the grain size of sample H in the in-plane direction at the interface, resulting in larger grains on the surface of the epitaxial film.

4. Conclusion

In this study, we attempted experiments to enhance the crystallinity and MO effect of Bi2.5:NIG thin films by introducing BIG underlayer. First, by investigating NIG/BIG films, we confirmed that the BIG underlayer could crystallize at 640 °C through interdiffusion between BIG underlayer and NIG layer. The distance for interdiffusion was around 25 nm. This experiment provided feasibility for the preparation of Bi2.5:NIG/BIG film. On glass and GGG (100) substrates, by introducing BIG underlayer, Bi2.5:NIG/BIG films exhibit an improved crystallinity and MO effects compared to Bi2.5:NIG films. The Faraday rotation angle at around 520 nm significantly increased from 16.7°/μm to 31.5°/μm on glass substrates and from 18.5°/μm to 27.8°/μm on GGG substrates. Simulation of the Faraday spectra indicate that the enhancement in MO effect of the film structure is due not only to the increased concentration of Bi^{3+} but also an improvement in the MO effect of the Bi2.5:NIG layer. By examining the cross-sectional and surface structures, we observed that Bi2.5:NIG/BIG film exhibits larger grain size on surface and fewer pores at the interface. This suggests that the introduction of BIG underlayer increases the mutual diffusions of Nd^{3+} and Bi^{3+} and promotes crystal growth at the interface, leading to an enhancement in the crystallinity and MO effects of the Bi2.5:NIG/BIG film.

Acknowledgements A part of this research was conducted with the joint research with the Nagoya University Institute for Advanced Research, and the Yamaguchi University Nanotechnology Microfabrication

Platform (F-21-YA-0015).

References

1) C. F. Buhrer: *J. Appl. Phys.*, **40**, 4500 (1969).
2) E. Jesenska, T. Yoshida, K. Shinozaki, T. Ishibashi, L. Beran, M. Zahradnik, R. Antos, M. Kučera, and M. Veis: *Opt. Mater. Express*, **6**, 1986 (2016).
3) S. Wittekoek, T. J. A. Popma, J. M. Robertson, and P. F. Bongers: *Phys. Rev. B*, **12**, 2777 (1975).
4) H. Takeuchi, K. Shinagawa, and S. Taniguchi: *J. Appl. Phys.*, **12**, 465 (1973).
5) P. Hansen and J.-P. Krumme: *Thin Solid Films*, **114**, 69 (1984).
6) T. Ishikawa, T. Masumoto, S. Ono, and K. Shiroki: *J. Magn. Soc. Jpn.*, **11**, 353 (1987).
7) K. Aoshima, N. Funabashi, K. Machida, Y. Miyamoto, K. Kuga, T. Ishibashi, N. Shimidzu, and F. Sato: *J. Dis. Tech.*, **6**, 374 (2010).
8) A. Tsuzuki, H. Uchida, H. Takagi, P. B. Lim, and M. Inoue: *J. Magn.*, **11**, 143 (2006).
9) T. Ishibashi, G. Lou, A. Meguro, T. Hashinaka, M. Sasaki, and T. Nishi: *Sensor Mater.*, **27**, 965 (2015).
10) Y. Nagakubo, Y. Baba, Q. Liu, G. Lou, and T. Ishibashi: *J. Magn. Soc. Jpn.*, **41**, 29 (2016).
11) Y. Nagakubo, Q. Liu, G. Lou, and T. Ishibashi: *AIP Advances*, **7**, 056803 (2017).
12) T. Ishibashi, *J. Magn. Soc. Jpn.*, **44**, 108 (2020).
13) T. Ishibashi, T. Kawata, T. H. Johansen, J. He, N. Harada, and K. Sato: *J. Magn. Soc. Jpn.*, **32**, 150 (2008).
14) M. Sasaki, G. Lou, Q. Liu, M. Ninomiya, T. Kato, S. Iwata, and T. Ishibashi: *J. Appl. Phys.*, **55**, 5501 (2016).
15) S. Ikehara, K. Wada, T. Kobayashi, S. Goto, T. Yoshida, T. Ishibashi, and T. Nishi: *J. Magn. Soc. Jpn.*, **36**, 169 (2012).
16) T. Yoshida, K. Oishi, T. Nishi and T. Ishibashi: *EPJ Web of Conferences*, **75**, (2014).
17) G. Lou, T. Kato, S. Iwata and T. Ishibashi: *Opt. Mater. Express*, **7**, 2248 (2017).
18) A. M. Grishin, S. I. Khartsev, and S. Bonetti: *Appl. Phys. Lett.,* **88**, 242504 (2006).
19) P. Hansen, K. Witter, and W. Tolksdorf: *Phys. Rev. B*, **27**, 6608 (1983).
20) N. Katagiri, N. Adachi, K. Yogo, K. Watanabe, S. Awata, and T. Ota: *Trans. Mat. Res. Soc. Jpn.*, **38**, 269 (2013).
21) T. Ishibashi, G. Lou, A. Meguro, T. Hashinaka, M. Sasaki, and T. Nishi: *Sens. Mater.*, **27**, 965 (2015).
22) T. Ishibashi, A. Mizusawa, M. Nagai, S. Shimizu, and K. Sato: *J. Appl. Phys.*, **97**, 013516 (2005).
23) R. Takahashi, Y. Yonezawa, M. Ohtani, M. Kawasaki, K. Nakajima, T. Chikyow, H. Koinuma, and Y. Matsumoto: *Adv. Funct. Mater.*, **16**, 485 (2006).
24) Akira Kawano, Ichiro Konomi, Hirozumi Azuma, Tatsumi Hioki, and Shoji Noda: *J. Appl. Phys.*, **74**, 4265 (1993).
25) K. Matsumoto, S. Sasaki, K. Haraga, K. Yamaguchi, and T. Fujii: *J. Appl. Phys.*, **71**, 2467 (1992).
26) H. Toraya and T. Okuda: *J. Phys. Chem. Sol.*, **56**, 1317 (1995).
27) Y. Xiong, M. Wu, Z. Peng, N. Jiang, and Q. Chen: *Chem. Lett.*, **33**, 502 (2004).
28) T. Kosaka, M. Naganuma, M. Aoyagi, T. Kobayashi, S. Niratisairak, T. Nomura, and T. Ishibashi: *J. Magn. Soc. Jpn.*, **35**, 194 (2011).
29) B. Bhoi, N. Venkataramani, R. P. R. C. Aiyar, S. Prasad, and M. Kostylev: *IEEE Trans. Magn.*, **54**, 2801205 (2018).
30) Y.-M. Kang, S.-H. Wee, S.-I. Baik, S.-G. Min, S.-C. Yu, S.-H. Moon, Y.-W. Kim, and S.-I. Yoo: *J. Appl. Phys.*, **97**, 10A319 (2005).
31) Y. Sun, Y.-Y. Song, H. Chang, M. Kabatek, M. Jantz, W. Schneider, M. Wu, H. Schultheiss, and A. Hoffmann: *Appl. Phys. Lett.*, **101**, 152405 (2012).
32) S. Visnovsky: Optics in Magnetic Multilayers and Nanostructures, CRC Press, Boca Raton, (2006).

Received Feb. 06, 2025; Revised Apr. 01, 2025; Accepted Sep. 16, 2025

Editorial Committee Members・Paper Committee Members

T. Taniyama and S. Okamoto (Chairperson), D. Oyama, M. Ohtake, T. Nozaki, and H. Kikuchi (Secretary)
H. Aoki　M. Goto　T. Goto　S. Haku　T. Hasegawa　R. Hashimoto
M. Iwai　T. Kawaguchi　T. Kawai　K. Kobayashi　T. Kojima　H. Kura
S. Muroga　T. Narita　M. Sakakibara　Y. Sato　E. Shikoh　Y. Shiota
T. Shirokura　S. Sugahara　K. Suzuki　Y. Takamura　T. Takura　S. Tamaru
M. Toko　S. Yakata　S. Yamada　T. Yamazaki　A. Yao　T. Yoshida
Y. Yoshida

N. Adachi　S. Ajia　F. Akagi　K. Bessho　A. Chikamatsu　M. Doi
T. Doi　T. Fukushima　Y. Hane　K. Hioki　S. Honda　S. Iihama
S. Isogami　N. Kikuchi　A. Kuwahata　T. Maki　K. Masuda　M. Naoe
K. Nawa　D. Oshima　S. Ota　R. Sakagami　S. Sakurai　Y. Sasaki
M. Sato　S. Seino　M. Sekino　T. Suetsuna　I. Tagawa　K. Tajima
M. Takezawa　T. Yamada　T. Yamazaki　S. Yoshimura

Notice for Photocopying

The Magnetics Society of Japan authorized Japan Academic Association For Copyright Clearance (JAC) to license our reproduction rights, reuse rights and AI ML rights of copyrighted works.
If you wish to obtain permissions of these rights in the countries or regions outside Japan, please refer to the homepage of JAC (http://www.jaacc.org/en/) and confirm appropriate organizations to request permission.
However, if CC BY 4.0 license icon is indicated in the paper, the Magnetics Society of Japan allows anyone to reuse the papers published under the Creative Commons Attribution International License (CC BY 4.0).
Link to the Creative Commons license: http://creativecommons.org/licenses/by/4.0/
Legal codes of CC BY 4.0: http://creativecommons.org/licenses/by/4.0/legalcode

編集委員・論文委員

谷山智康（理事）　岡本 聡（理事）　小山大介（幹事）　大竹 充（幹事）　野崎友大（幹事）　菊池弘昭（特任幹事）
青木英恵　岩井守生　川井哲郎　川口昂彦　藏 裕彰　小嶋隆幸　後藤太一　後藤 穣　小林宏一郎
榊原 満　佐藤佑樹　塩田陽一　仕幸英治　白倉孝典　菅原 聡　鈴木和也　高村陽太　田倉哲也
田丸慎吾　都甲 大　成田正敬　白 怜士　橋本良介　長谷川崇　室賀 翔　八尾 惇　家形 諭
山崎貴大　山田晋也　吉田 敬　吉田征弘

阿加賽見　赤城文子　安達信泰　飯浜賢志　磯上慎二　大島大輝　大多哲史　菊地伸明　桑波田晃弘
坂上良介　櫻井 将　佐々木悠太　佐藤光秀　末綱倫浩　清野智史　関野正樹　田河育也　竹澤昌晃
田島克文　近松 彰　土井達也　土井正晶　直江正幸　名和憲嗣　羽根吉紀　日置敬子　福島隆之
別所和宏　本多周大　槙 智仁　増田啓介　山崎 匠　山田豊和　吉村 哲

複写をされる方へ

当学会では，複写複製，転載複製及びAI利用に係る著作権を一般社団法人学術著作権協会に委託しています.
当該利用をご希望の方は，(社)学術著作権協会（https://www.jaacc.org/）が提供している許諾システムを通じてご申請下さい.

ただし，クリエイティブ・コモンズ [表示 4.0 国際] (CC BY 4.0)の表示が付されている論文を，そのライセンス条件の範囲内で再利用する場合には，本学会からの許諾を必要としません.
クリエイティブ・コモンズ・ライセンス http://creativecommons.org/licenses/by/4.0
リーガルコード http://creativecommons.org/licenses/by/4.0/legalcode.ja

---

Journal of the Magnetics Society of Japan
Vol. 50 No. 1 (通巻第343号) 2026年1月1日発行

Vol. 50 No. 1 Published Jan. 1, 2026
by the Magnetics Society of Japan
Tokyo YWCA building Rm207, 1–8–11 Kanda surugadai, Chiyoda-ku, Tokyo 101–0062
Tel. +81–3–5281–0106　Fax. +81–3–5281–0107

Printed by JPC Co., Ltd.
Sports Plaza building 401, 2–4–3, Shinkamata Ota-ku, Tokyo 144–0054
Advertising agency: Kagaku Gijutsu-sha

発行：（公社）日本磁気学会　101–0062　東京都千代田区神田駿河台 1–8–11　東京YWCA会館 207 号室
製作：ジェイピーシー　144–0054　東京都大田区新蒲田 2–4–3　スポーツプラザビル401　Tel.（03）6715–7915
広告取扱い：科学技術社　111–0052　東京都台東区柳橋 2–10–8　武田ビル4F　Tel.（03）5809–1132

Copyright　©2026 by the Magnetics Society of Japan